Chemodynamical study of two CEMP-no stars from the Hamburg/ESO Survey

J. Shejeelammal[1,2] and Aruna Goswami[1,3]★

[1]*Indian Institute of Astrophysics, Koramangala, Bangalore 560034, India*
[2]*Departamento de Astronomia, Universidade de São Paulo, Instituto de Astronomia, Geofísica e Ciências Atmosféricas, IAG, Rua do Matão 1226, Cidade Universitária, 05508-900 São Paulo, Brazil*
[3]*Institute of Frontier Science and Application, Bangalore 560037, India*

ABSTRACT

The Carbon-Enhanced Metal-Poor (CEMP) stars with no enhancement of neutron-capture elements, the so-called CEMP-no stars are believed to be the direct descendants of first-generation stars and provide a unique opportunity to probe the early Galactic nucleosynthesis. We present a detailed chemical and kinematic analysis for two extremely metal-poor stars HE 1243 − 2408 and HE 0038 − 0345 using high-resolution (R∼86 000) HERMES spectra. For the object HE 1243 − 2408, we could make a detailed comparison with the available literature values; however, only limited information is available for the other object HE 0038 − 0345. Our estimated metallicity for these two objects are −3.05 and −2.92, respectively. With estimated [C/Fe] (1.03 and 1.05) and [Ba/Fe] (−0.18 and −0.11), respectively, the objects are found to be bonafide CEMP-no stars. From the observed abundances of C, Na, Mg, and Ba (i.e. A(C), A(Na), A(Mg), A(Ba)), the objects are found to belong to Group II CEMP-no stars. A detailed abundance profile analysis indicates that the objects are accreted from dSph satellite galaxies that support hierarchical galaxy assembly. Further, our analysis shows that the progenitors of the stars are likely Pop II Core-Collapse Supernovae. The object HE 0038 − 0345 is found to be a high-energy, prograde, outer-halo object, and HE 1243 − 2408 is found to be a high-energy, retrograde, inner-halo object. Our detailed chemodynamical analysis shows that HE 1243 − 2408 is related to I'itoi structure, where as HE 0038 − 0345 is likely related to Sgr or GSE events. The mass of the progenitor galaxies of the programme stars inferred from their dynamics is at par with their likely origin in massive dSph galaxies.

Key words: stars: carbon – stars: abundances – stars: chemically peculiar – stars: individual – stars: kinematics and dynamics.

1 INTRODUCTION

The CEMP-no stars, a sub-class of Carbon-Enhanced Metal-Poor (CEMP) stars with enhanced carbon abundance and no signatures of heavy neutron-capture elements, are the most chemically primitive objects presently known (Norris & Yong 2019; Yoon et al. 2020). These stars occupy the lowest metallicity tail ([Fe/H]<−3) of the Metallicity Distribution Function (MDF) of the galaxy (Yong et al. 2013; de Bennassuti et al. 2017; Norris & Yong 2019; Yoon et al. 2019), and their fraction increases with decreasing metallicity, constituting ∼20 per cent of very metal-poor stars ([Fe/H]<−2), ∼40 per cent of extremely metal-poor stars ([Fe/H]<−3), and ∼75 per cent of ultra metal-poor (UMP) stars ([Fe/H]<−4) (Frebel et al. 2006; Carollo et al. 2012; Lee et al. 2013; Placco et al. 2014; Banerjee, Qian & Heger 2018). Among the 14 known CEMP stars with [Fe/H]<−4.5, 12 stars belong to the CEMP-no group, and they might have been formed a few million years after the big bang (Norris & Yong 2019). They are formed from the ejecta of the first-generation, massive, short-lived Pop III stars (Frebel et al. 2008; Nomoto, Kobayashi & Tominaga 2013; Spite et al. 2013; Placco et al. 2014; Choplin et al. 2017; Ezzeddine et al. 2019). The indirect

studies of the formation and nucleosynthesis pathways of the first stars, and their contribution to the early chemical enrichment of the universe, can be achieved through the analysis of chemical imprints of their direct descendants, the CEMP-no stars (Hansen et al. 2016a; Yoon et al. 2019). Hence, the CEMP-no stars are important probes in studies of Galactic archaeology that aims to understand the nature of the first generation stars, the associated nucleosynthesis, the early star formation and galaxy formation, and early Galactic chemical evolution etc. (Bonifacio et al. 2015; Frebel & Norris 2015; Hansen et al. 2016a; Yoon et al. 2020). Further, these stars are expected to shed light on the physical processes resulting in the transitions from massive Pop III stars to normal Pop II stars (Salvadori, Schneider & Ferrara 2007; Hartwig et al. 2015; de Bennassuti et al. 2017).

Different scenarios have been suggested by various authors for the origin of CEMP-no stars (Hansen et al. 2015, Yoon et al. 2016 and references there in), however, the exact origin of these stars still remains unknown. According to some authors, the CEMP-no stars are generally single stars, suggesting an intrinsic origin, that is, formed from a pre-enriched natal cloud of ISM (Spite et al. 2013; Starkenburg et al. 2014; Bonifacio et al. 2015; Yoon et al. 2016; Hansen et al. 2016b). The suggested progenitors for the CEMP-no stars include (i) faint supernovae that underwent mixing and fall back. Due to the low explosion energy, such SNe could not expel all the

★ E-mail: shejeela@usp.br (JS); aruna@iiap.res.in (AG)

synthesized element. Only the light elements such as C, N, O, Na, Mg, Al, and Si are released to the ISM (Umeda & Nomoto 2003, 2005; Tominaga, Iwamoto & Nomoto 2014), (ii) extremely metal-poor fast rotating massive stars or spinstars that enriched the ISM with C, N, and O through strong stellar winds (Meynet, Ekström & Maeder 2006; Frischknecht, Hirschi & Thielemann 2012; Maeder & Meynet 2015; Choplin et al. 2017), and (iii) i-process in massive Pop III stars (Clarkson, Herwig & Pignatari 2018). In addition to these scenarios, Arentsen et al. (2019) suggested that the binary mass-transfer from extremely metal-poor AGB companion stars in the past might explain at least a few of the CEMP-no stars among the confirmed binary CEMP-no objects. If the binary-mass-transfer scenario holds true for the origin of CEMP-no stars, this will help to understand extremely metal-poor AGB stars and provide robust observational constraints to the AGB nucleosynthesis and mass-transfer models for metallicity [Fe/H]<-2.

The differences in the morphology of CEMP-no stars on the Yoon – Beers diagram (A(C) – [Fe/H] diagram) leading to two distinct groups, Group II and Group III CEMP-no stars, suggest multiple formation pathways for them (Yoon et al. 2016). In addition to these two groups of CEMP-no stars, a few of the CEMP-no stars ($\sim$ 15 per cent) are found to lie in the high-carbon region that is typically occupied by CEMP-s and CEMP-r/s stars (Group I), known as Group I CEMP-no stars. However, these CEMP-no stars show larger [Sr/Ba] values than those in the Group I CEMP-s and CEMP-r/s stars (Norris & Yong 2019). Eight objects among these Group I CEMP-no stars are confirmed binaries (Yoon et al. 2016, Arentsen et al. 2019 and references therein). Similarity in the morphology of the Yoon – Beers diagram for the CEMP-no stars in the Galactic halo and dwarf satellite galaxies suggested that the halo CEMP-no stars are accreted from the mini halos (Bonifacio et al. 2015; Yoon et al. 2018, 2019, 2020). Additional spectroscopic studies of Group I, Group II, and Group III CEMP-no stars in both the galaxy and its satellite galaxies are required to better constrain their origin, and hence the nature of first stars. In addition to this, such studies will help us to improve our understanding of Galactic assembly and Galactic halo formation. Further study is required to investigate what fraction of these anomalous Group I CEMP-no stars are binaries, and also to explain the origin of binary CEMP-no stars with low carbon abundance.

Several cosmological simulations are in accordance with the hierarchical Galactic halo assembly through numerous complex mergers (e.g. Deason et al. 2013; Pillepich et al. 2014; Amorisco 2017). The highly structured nature of the Galactic halo points at an accretion origin. This has simulated several high- and medium-resolution spectroscopic studies of different samples (Myeong et al. 2019; Naidu et al. 2020; Aguado et al. 2021; Woody & Schlaufman 2021; Malhan et al. 2022; Zepeda et al. 2023), and large-scale surveys (e.g. GALAH; Buder et al. 2018). Based on high-precision data from the *Gaia* Satellite, these studies identified various structures arising from the clustering of satellite galaxies, stellar streams, and globular clusters in the dynamic (Energy – Action) space, and attempted to uncover the Milky Way mergers. These structures in various chemical and dynamical planes, along with the observations of r-process stars in the halo, revealed the signatures of remnants of dwarf satellite galaxies accreted in the past by the galaxy, and unambiguously confirmed the importance of accretion for its formation (Myeong et al. 2018; Roederer et al. 2018; Dietz et al. 2020; Helmi 2020; Woody & Schlaufman 2021; Malhan et al. 2022; Naidu et al. 2022; Frebel & Ji 2023; Zepeda et al. 2023). It has been shown that the massive progenitor dwarf galaxies ($M_\star \geq 10^8 - 10^9\,M_\odot$) contribute primarily to the accreted halo, with sub-dominant contributions from

the low-mass satellite galaxies (Dietz et al. 2020; Naidu et al. 2020). Major massive dwarf satellite galaxy accretions that built the Galactic halo are *Gaia*-Sausage-Enceladus (GSE; Belokurov et al. 2018; Helmi et al. 2018), Kraken/Koala/Heracles (Kruijssen et al. 2019; Forbes 2020; Horta et al. 2021; Pfeffer et al. 2021), and Sequoia (Matsuno, Aoki & Suda 2019; Myeong et al. 2019). These events happened $\sim$10 Gyr ago at red-shifts z$\simeq$2, with more than 50 per cent of the halo stars in the solar neighbourhood coming from the GSE (Helmi et al. 2018; Kruijssen et al. 2019; Frebel & Ji 2023). Besides these major mergers, several other numerous minor accretions (both massive and low-mass) like Aleph, Arjuna, I'itoi, Wukong/LMS-1 (Naidu et al. 2020), Thamnos (Koppelman et al. 2019) etc. have contributed to the Galactic halo.

Although it is known that numerous dwarf satellite galaxy accretions led to the formation of the present-day Milky Way halo, our understanding of this process is still lacking, particularly in terms of the total number of mergers, their dynamical characteristics, and their contributions to various stellar populations of the halo (Malhan et al. 2022; Frebel & Ji 2023). Since many metal-poor stars in the halo trace their origin to the dwarf satellite galaxies (Frebel & Norris 2015; Frebel & Ji 2023), they are ideal tools to study the Galactic halo assembly. Based on the kinematic, chemical, and dynamical properties of a sample of 644 CEMP stars, Zepeda et al. (2023) have shown that the CEMP-no stars are not *in situ* to the galaxy, but were originally born in satellite galaxies that were accreted and disrupted by the Milky Way. This is also on par with the findings of Yoon et al. (2019). Several authors have discussed the relevance and scope of enhancing medium- and high-resolution spectroscopic studies of different sub-groups of CEMP-no stars to further our understanding of early Galactic chemical evolution and Galactic halo formation (eg. Hansen et al. 2015, 2016c; Norris & Yong 2019; Yoon et al. 2019, 2020; Zepeda et al. 2023). The stars that were accreted very early into the galaxy still retain their original chemical composition and a few kinematic properties such as energy, action, and angular momentum (Frebel & Ji 2023). Zepeda et al. (2023) have discussed the possibility of recovering the Galactic accretion events through a clustering approach, and matching the chemical, orbital, and kinematic properties of CEMP stars with each other. Along this line, we have conducted a high-resolution spectroscopic and chemodynamical analysis of two CEMP-no stars, HE 0038 − 0345 and HE 1243 − 2408, with the aim of deriving clues to their origin.

This paper is arranged as follows. A brief discussion on previous studies of the stellar sample is given Section 2. Section 3 describes the method of sample selection, data acquisition and data reduction. Estimation of radial velocity is given in Section 4, followed by the description of stellar atmospheric parameter estimation and mass determination in Section 5. Section 6 provides procedures adopted for abundance determination. Abundance uncertainty is given in Section 7. A detailed discussion on the abundance pattern and the progenitors of the programme stars is presented in Section 8. Kinematic analysis of the sample is given in Section 9. A detailed discussion on the orbital and various dynamical properties of the programme stars in the galaxy is also provided in this section. In Section 10, we have discussed our chemodynamical analysis to assign the stars to known accretion structures of Milky Way. Finally, the conclusions are summarized in Section 11.

2 PREVIOUS STUDIES ON THE PROGRAMME STARS: A BRIEF SUMMARY

Based on an analysis of medium-resolution spectra ($\sim$ 2 Å) obtained with 2–4 m class telescopes, Frebel et al. (2006) derived metallicity

of the programme stars as -2.86 and -2.88 for HE 0038 $-$ 0345 and HE 1243 $-$ 2408, respectively, and carbon abundance with respect to iron [C/Fe], as 0.3 and 0.13, respectively. Their classification as metal-poor stars were determined by applying a selection procedure taking account the strength of the Ca II K line as a function of the metallicity and the effective temperature. The strength of Ca II K line is measured following the procedure in Beers (1999) by means of the line index KP, a pseudo-equivalent width measurement in Å. Ca II K line is known as the strongest metal absorption line in the optical wavelength range. The optical photometry by Beers et al. (2007) gave B$-$V = 0.767 with E(B$-$V) = $+0.043$ for the object HE 0038 $-$ 0345. Beers et al. (2017) also derived the metallicity [Fe/H] and carbonicity [C/Fe] of these objects as ($-2.51, 0.76$) and ($-2.65, 0.75$) for HE 0038 $-$ 0345 and HE 1243 $-$ 2408, respectively, based on medium-resolution spectral analysis, and classified them as CEMP-no stars. The wavelength regions used as inputs to the n-SSPP (non-SEGUE Stellar Parameter Pipeline) for determination of the parameters span a range of 3600–4400, 3600–4800, or 3600–5250 Å.

Using spectral synthesis calculations, Holmbeck et al. (2020) derived the metallicity [Fe/H] ($-$ 2.53) and abundances of C, Sr, Ba, and Eu for the object HE 0038 $-$ 0345, based on a snapshot high-resolution spectrum of HE 0038–0345 at a resolution$\sim$30 000 with a SNR$\sim$30. While carbon is found to be mildly enhanced with [C/Fe] = 0.46, Sr and Ba are found below solar with [Sr/Fe] = -0.16 and [Ba/Fe] = -0.49. The abundance of Eu is however found as near-solar with [Eu/Fe] = 0.12. The object is classified as a non-RPE (no r-process enhancement) star (Holmbeck et al. 2020). Our estimates of effective temperature and surface gravity match closely with those of Holmbeck et al. (2020) within the error limits. However, we got lower values for the micro-turbulent velocity ($\Delta\sim$1.43 km s^{-1}) and metallicity ($\Delta\sim$0.39 dex) compared to them.

Among the Fe I and II lines used for stellar atmospheric parameter determination, four Fe I lines 4889.74, 5339.93, 5393.17, 5586.76 Å, and one Fe II line 4520.224 Å are common with those used by Holmbeck et al. (2020). In Holmbeck et al. (2020), the measured equivalent widths of these Fe I lines are almost double, and that of the Fe II line is almost 7 times as large as that measured by us. Besides, among the 84 Fe I lines used by them, 26 lines are with excitation potentials, $E_{low} < 1.2$ eV. In EMP stars, the Fe I lines with $E_{low} < 1.2$ eV are affected by 3D hydrodynamic effects and show significant deviation from 1D (Tafelmeyer et al. 2010; Hayek et al. 2011; Dobrovolskas et al. 2013; Jablonka et al. 2015). The abundances estimated from these lines are shown to be over-estimated (Collet, Asplund & Trampedach 2007; Dobrovolskas et al. 2013; Mashonkina et al. 2017). For instance, in the analysis of Collet, Asplund & Trampedach (2007), in the T_{eff}/log g/[Fe/H] $\sim$ 4858/2.2/-3 model, the Fe I line with $E_{low} = 0$ eV gave an abundance $\sim$0.8 dex higher compared to the Fe I line with $E_{low} = 4$ eV, whereas Mashonkina et al. (2017) noted a difference of $\sim$0.36 dex, Dobrovolskas et al. (2013) noted $\sim$0.5 dex. Since 30 per cent of the Fe I lines used by Holmbeck et al. (2020) are low E_{low} lines, the Fe abundance could likely be over-estimated.

Based on a VLT/UVES spectrum at resolution 40 000 and SNR$\sim$130, Lombardo et al. (2022) have performed an analysis of the object HE 1243–2408, and presented the stellar atmospheric parameters and elemental abundances of 15 elements. Our estimates of stellar atmospheric parameters are lower compared to Lombardo et al. (2022); Δ(T_{eff}, log g, ζ, [Fe/H]) $\sim$ (223 K, 0.95, 0.74 km s^{-1}, 0.2). Though the analysis in both cases is based on 1D LTE, the adopted procedures and methodologies are different. The differences in the method of estimation of stellar atmospheric parameters and

elemental abundances, differences in the choices of atomic data, solar abundance values, Fe partition functions etc. could affect the derived values (Roederer et al. 2018). While we have derived the stellar atmospheric parameters spectroscopically using the traditional excitation, ionization balances of Fe I – Fe II lines, Lombardo et al. (2022) used the *Gaia* EDR3 photometry and parallax values, following the procedure in Koch-Hansen et al. (2021). The micro-turbulent velocity is estimated using a calibration equation from Mashonkina et al. (2017). The micro-turbulent velocity estimated this way is shown to exhibit a discrepancy of ±0.5 km s^{-1} from the spectroscopic value, reaching up-to a value of $\sim$0.7 km s^{-1} (Mashonkina et al. 2017). The analysis of Mucciarelli & Bonifacio (2020) has shown that the photometric estimates of atmospheric parameters are higher than the spectroscopic ones, and the deviation increases with decreasing metallicity. At [Fe/H]~-2.5, the photometric temperature and surface gravity are higher than the spectroscopic values by $\sim$350 K and $\sim$1.0 dex, respectively (Mucciarelli & Bonifacio 2020). This is in agreement with the discrepancy observed in the estimates of Lombardo et al. (2022) and other studies in the literature. This could be likely due to the 3D and/or NLTE effects in the lower metallicity, which leads to the non-zero slope in the excitation potential and observed Fe abundances when using the photmetric temperature (Mucciarelli & Bonifacio 2020; Koch-Hansen et al. 2021; Lombardo et al. 2022). However, current modelling of the giant stars incorporating these effects could not remove this slope completely (Mucciarelli & Bonifacio 2020). Finally, the discrepancy in the estimates of stellar atmospheric parameters between our study and that of Lombardo et al. (2022) is reflected in the estimates of elemental abundances as well.

## 3 STELLAR SPECTRA: OBJECT SELECTION, OBSERVATION, AND DATA REDUCTION

The programme stars, HE 0038 $-$ 0345 and HE 1243 $-$ 2408, are selected from the catalogue of bright (13 < B < 14.5) metal-poor candidates (Frebel et al. 2006) from the Hamburg/ESO Survey (HES). The high-resolution spectra of the objects were acquired using the High-Efficiency and high-Resolution Mercator Echelle Spectrograph (HERMES) attached to the 1.2-m Mercator telescope at the Roque de los Muchachos Observatory in La Palma, Canary Islands, Spain (Raskin et al. 2011). The spectra cover the wavelength range 3770–9000 Å, and have resolution R$\sim$86 000. For the object HE 0038 $-$ 0345, three frames with exposures 2000, 700, and 1600 s were taken on 2018 December 10, 2019 January 29, and 2019 October 31, respectively. In the case of HE 1243 $-$ 2408, two frames of 1400 s exposures were taken on 2019 February 02. The spectra were reduced using the HERMES pipeline. Multiple frames for each object are co-added after the Doppler correction, to enhance the S/N ratio. The co-added spectra are continuum fitted using IRAF (Image Reduction and Analysis Facility) software. The basic data of the programme stars are given in Table 1. A small portion of the continuum-fitted, radial-velocity-corrected spectra of the stars are shown in Fig. 1 as an example.

4 RADIAL VELOCITY

The radial velocities of the programme stars are estimated from the measured shift in wavelengths of several clean and unblended spectral lines, using the standard procedure as discussed in Shejeelammal & Goswami (2022). The average of the radial velocities for each object corrected for heliocentric motion is taken as the radial velocity of the object. The detailed radial velocity data of the objects

Table 1. Basic information of the programme stars.

| Star | RA (2000) | Dec. (2000) | B | V | J | H | K | S/N | | |
								4200 Å	5500 Å	7700 Å
HE 0038 − 0345	00 41 09.29	−03 28 59.51	11.99	11.30	9.886	9.419	9.293	15.08	58.67	74.86
HE 1243 − 2408	12 45 53.85	−24 25 02.42	11.66	10.97	9.075	8.551	8.434	13.55	56.41	65.01
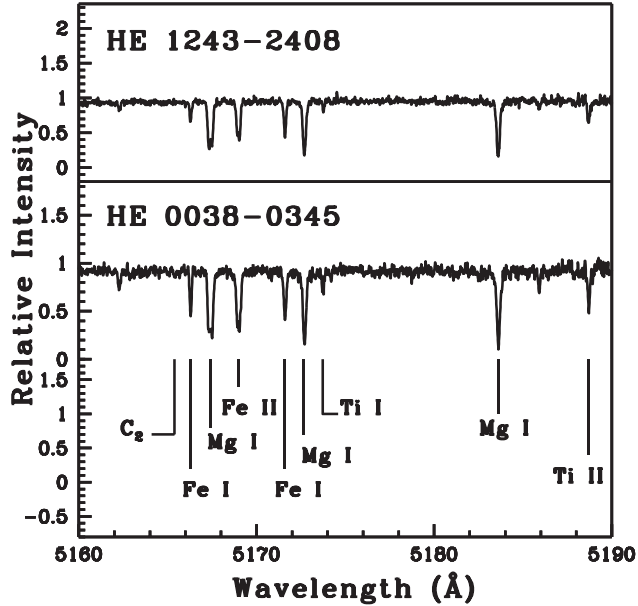
Figure 1. Sample spectra of the programme stars in the wavelength region 5160 – 5190 Å.

will be published in a summary paper (Jorissen et al., in preparation) on the orbits of CEMP stars. Our radial velocity estimates, along with those from *Gaia* DR3 (*Gaia* Collaboration et al. 2022) are presented in Table 2. Our radial velocity values for these two objects match quite closely with *Gaia* values.

5 STELLAR ATMOSPHERIC PARAMETERS

The stellar atmospheric parameters are derived using the standard excitation balance and ionization balance methods from a set of clean lines of Fe I and Fe II (Appendix Table A1). We performed the analysis under the assumption of local thermodynamic equilibrium

(LTE), using the code MOOG (version 2013, Sneden 1973). The selected spectral lines have excitation potentials in the range 0–6 eV and equivalent widths in the range 5–180 mÅ. The model atmospheres are selected from the Kurucz grid of model atmospheres (Castelli & Kurucz 2003, http://kurucz.harvard.edu/grids.html). We have followed the detailed procedure for stellar atmospheric parameter estimation as discussed in our earlier papers Shejeelammal et al. (2020); Shejeelammal & Goswami (2021); Shejeelammal, Goswami & Shi (2021). By setting the slope of the estimated Fe I abundances with excitation potentials to zero, the effective surface temperature is obtained. The micro-turbulent velocity is then derived by establishing a zero trend between the abundances of Fe I lines and their reduced equivalent widths. Lastly, by adjusting its value until the abundances of the Fe I and Fe II lines coincide, the surface gravity is determined. To derive the final stellar atmospheric parameters, an iterative process is performed until these three conditions are simultaneously accomplished. The derived stellar atmospheric parameters of the stars, along with the literature values are given in Table 2. The iron abundances derived from different Fe I and Fe II lines are shown in Fig. 2.

The surface gravity of the programme stars are estimated from the parallax method as well. The log g values are calculated using the equation $\log (g/g_\odot) = \log (M/M_\odot) + 4 \log (T_{\rm eff}/T_{\rm eff\odot}) - \log (L/L_\odot)$, where $T_{\rm eff\odot} = 5770$ K, $\log g_\odot = 4.44$, and $M_{\rm bol\odot} = 4.74$ mag (Bessell, Castelli & Plez 1998). The stellar masses are determined from the position on the H-R diagram. We have adopted the stellar evolutionary tracks of Girardi et al. (2000) to generate the H-R diagrams. The detailed procedure followed is discussed in Shejeelammal et al. (2020). The positions of the programme stars on the H-R diagram are shown in Fig. 3. We have used z = 0.0004 tracks for this H-R diagram. We could not estimate the mass of the star HE 1243 − 2408 since the evolutionary tracks corresponding to its luminosity and temperature are not available. The estimated mass of the object HE 0038 − 0345 is $0.60 \pm 0.05\,M_\odot$ and the log g value is 1.68. The spectroscopic surface gravity value of this star match closely with that derived from the parallax method within

Table 2. Derived atmospheric parameters and radial velocity of the programme stars.

Star	$T_{\rm eff}$ (K) ±100	log g cgs ±0.2	ζ (km s⁻¹) ±0.2	[Fe I/H]	[Fe II/H]	V_r† (km s⁻¹) (This work)	V_r (km s⁻¹) (*Gaia* DR3)	Reference
HE 0038 − 0345	4830	1.75	0.78	−2.92 ± 0.07	−2.92 ± 0.03	−43.66 ± 0.05	−44.42 ± 0.84	1
	–	–	–	−2.86	–	–	–	2
	5010	1.82	–	−2.51	–	–	–	3
	4898	1.78	2.21	−2.53	–	–	–	4
HE 1243 − 2408	4800	1.40	0.98	−3.05 ± 0.12	−3.05 ± 0.12	+ 213.61 ± 0.03	+ 213.22 ± 0.21	1
	–	–	–	−2.88	–	–	–	2
	5293	2.13	–	−2.65	–	–	–	3
	5023	2.35	–	−2.85	–	–	–	5

Notes.† The numbers with the radial velocity values are standard deviations.
References: 1. Our work, 2. Frebel et al. (2006), 3. Beers et al. (2017), 4. Holmbeck et al. (2020), 5. Lombardo et al. (2022)
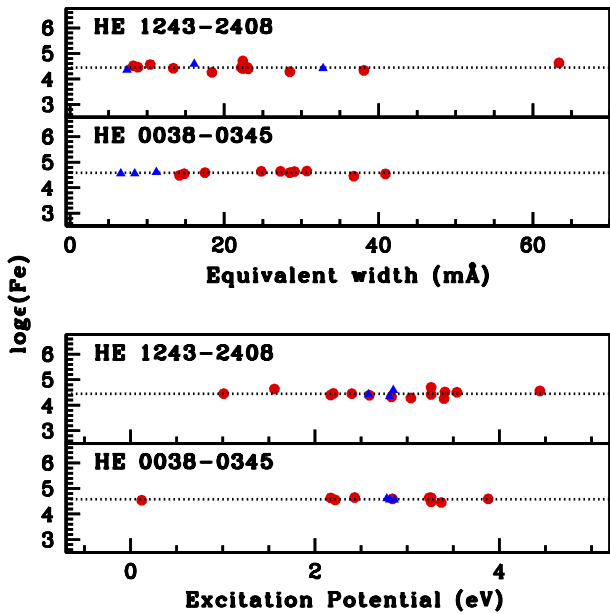
Figure 2. The estimated Fe I (solid circles) and Fe II (solid triangles) abundances of the programme stars with respect to (i) equivalent width (upper panel) and (ii) excitation potential (lower panel). The dotted lines in each panel is the adopted value of Fe abundance for the programme stars.
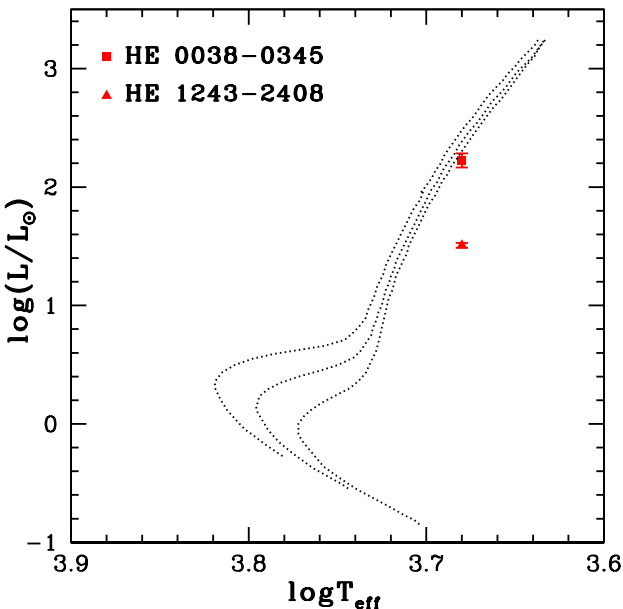

Figure 3. The evolutionary tracks for 0.6, 0.7, and 0.8 $M_\odot$ for z = 0.0004 are shown from bottom to top.

0.07 dex. We have adopted the spectroscopic surface gravity value for the analysis.

6 ABUNDANCE DETERMINATION

Abundances of different elements are determined using the measured equivalent widths of spectral lines as well as the spectrum synthesis method. For the elements with hyper-fine splitting (HFS) as well as for molecular bands, we have used spectrum synthesis

calculation. Different line parameters are taken from `linemake` (https://github.com/vmplacco/linemake) atomic and molecular line data base (Placco et al. 2021). The abundances are estimated relative to solar values (Asplund et al. 2009). The NLTE corrections are applied to the derived elemental abundances wherever applicable. The derived elemental abundances of the programme stars are given in Table 3. The lines used to derive the abundances are given in Appendix Tables A1 – A2.

6.1 Light elements: C, N, Na, α-, and Fe-peak elements

The carbon abundances are derived from the spectral synthesis calculation of CH G-band at 4315 Å. The derived [C/Fe] values with evolutionary corrections are 1.05 and 1.03 for HE 0038 − 0345 and HE 1243 − 2408, respectively. The other C_2 molecular bands are very weak and marginally detectable in the programme stars, and hence, could not be used for abundance analysis. The spectral synthesis fits for the CH band at 4315 Å are shown in Fig. 4.

The nitrogen abundance is derived from the spectrum synthesis calculation of ^{12}CN band at 4215 Å. Since this region of the spectra is noisy, the derived abundances are taken to be upper limits. Both the programme stars show enhanced abundances of nitrogen with [N/Fe] values <2.92 in HE 0038 − 0345, and <3.55 in HE 1243 − 2408.

The sodium abundances are derived from the spectrum synthesis calculation of Na I 5889.951, 5895.924 Å lines. The NLTE corrections to the abundances derived from these lines are adopted from Andrievsky et al. (2007), which are −0.53 and −0.41 for HE 0038 − 0345 and HE 1243 − 2408, respectively. In HE 0038 − 0345, we could derive the abundance of sodium from Na I 5682.63 Å line as well. While the object HE 0038 − 0345 shows a large enhancement in Na with [Na/Fe]∼0.85, the object HE 1243 − 2408 shows a moderate enhancement with [Na/Fe]∼0.43.

The abundances of Mg, Si, Ca, Ti, Cr, Ni, and Zn are derived from the measured equivalent widths of different spectral lines listed in Appendix Table A2. The abundance of magnesium is derived from the Mg I 4702.991, 5528.405 Å lines in both the programme stars. While Mg is enhanced in HE 0038 − 0345 with [Mg/Fe]∼0.67, the object HE 1243 − 2408 shows [Mg/Fe]∼0.84. The Si I 5948.541 Å line is used to derive the silicon abundance in HE 0038 − 0345 and found to be enhanced with [Si/Fe]∼0.82. No good Si lines usable for the abundance determination could be found in HE 1243 − 2408. In both stars, five Ca I lines (Appendix Table A2) are used to derive the calcium abundances. While the object HE 0038 − 0345 shows an abundance of Ca with [Ca/Fe]∼0.47, the object HE 1243 − 2408 shows moderate enhancement with [Ca/Fe]∼0.31. The abundance of scandium could only be estimated in the object HE 1243 − 2408, where we have used the spectral synthesis calculation of Sc II 5526.79 Å line. Scandium shows a mild enhancement ([Sc/Fe]∼0.15) in this object. We could not estimate the Sc abundance in the star HE 0038 − 0345 as there are no good lines. Both programme stars show moderate enhancement of Ti with values [Ti I/Fe]∼0.53 (HE 0038 − 0345) and 0.44 (HE 1243 − 2408). The abundance of Ti measured using Ti II lines also shows enhancement with [Ti II /Fe]≥0.40.

Chromium shows near-solar values in both the stars with [Cr/Fe]∼0.11 and −0.11 for HE 0038 − 0345 and HE 1243 − 2408, respectively. Nickel is also found to show near-solar values with [Ni/Fe]∼0.12 (HE 0038 − 0345) and [Ni/Fe]∼0.00 (HE 1243 − 2408). The Zn abundances are derived using the lines Zn I 4722.150 and 4810.530 Å for HE 0038 − 0345 and HE 1243 − 2408, respectively. Zinc is found to be moderately enhanced in both the objects with [Zn/Fe]∼0.56 and 0.37 for HE 0038 − 0345 and HE

Table 3. Elemental abundances in HE 0038 − 0345 and HE 1243 − 2408.

			HE 0038 − 0345			HE 1243 − 2408		
	Z	Solar logε*	logε	[X/H]	[X/Fe]	logε	[X/H]	[X/Fe]
C (CH band 4315 Å)†	6	8.43	6.43(syn)	−2.00	0.92 (1.05)	5.95(syn)	−2.48	0.57 (1.03)
N (^{12}CN band 4215 Å)	7	7.83	<7.83(syn)	<0.0	<2.92	<8.33(syn)	<0.5	<3.55
Na I_{NLTE}	11	6.24	4.17 (syn)(2)	−2.07	0.85	3.62 ± 0.09(syn)(2)	−2.62	0.43
Na I_{LTE}	11	6.24	4.20 (syn)(2)	−2.04	0.88	–	–	–
Mg I	12	7.6	5.35 ± 0.13(2)	−2.25	0.67	5.39 ± 0.13(2)	−2.21	0.84
Si I	14	7.51	5.41(1)	−2.10	0.82	–	–	–
Ca I	20	6.34	3.89 ± 0.19(5)	−2.45	0.47	3.60 ± 0.09(5)	−2.74	0.31
Sc II	21	3.15	–	–	–	0.25(syn)(1)	−2.90	0.15
Ti I	22	4.95	2.56 ± 0.15(3)	−2.39	0.53	2.34 ± 0.15(3)	−2.61	0.44
Ti II	22	4.95	2.58 ± 0.12(4)	−2.37	0.55	2.30 ± 0.16(3)	−2.65	0.40
Cr I	24	5.64	2.83 ± 0.20(2)	−2.81	0.11	2.48 ± 0.07(4)	−3.16	−0.11
Fe I	26	7.5	4.58 ± 0.07(10)	−2.92	–	4.45 ± 0.12(14)	−3.05	–
Fe II	26	7.5	4.58 ± 0.03(3)	−2.92	–	4.45 ± 0.12(3)	−3.05	–
Ni I	28	6.22	3.42 ± 0.06(2)	−2.80	0.12	3.17 ± 0.10(3)	−3.05	0.0
Zn I	30	4.56	2.20(1)	−2.36	0.56	1.88(1)	−2.68	0.37
Sr II	38	2.87	−0.87(syn)(1)	−3.74	−0.82	–	–	–
Y II	39	2.21	<−1.31(syn)(1)	<−3.52	<−0.60	−1.23(syn)(1)	−3.44	−0.39
Zr I	40	2.58	–	–	–	<−0.58(syn)(1)	<−3.16	<−0.11
Ba II	56	2.18	−0.85(syn)(1)	−3.03	−0.11	−1.05(syn)(1)	−3.23	−0.18
Eu II	63	0.52	<−1.82(syn)(1)	<−2.34	<0.58	–	–	–

Notes. ∗ Asplund et al. (2009), The number of lines used to derive the abundance are given in parenthesis.
NLTE refers to the abundance obtained after applying the NLTE correction.
† The values in the parenthesis for [C/Fe] are obtained after applying corrections for evolutionary effect.
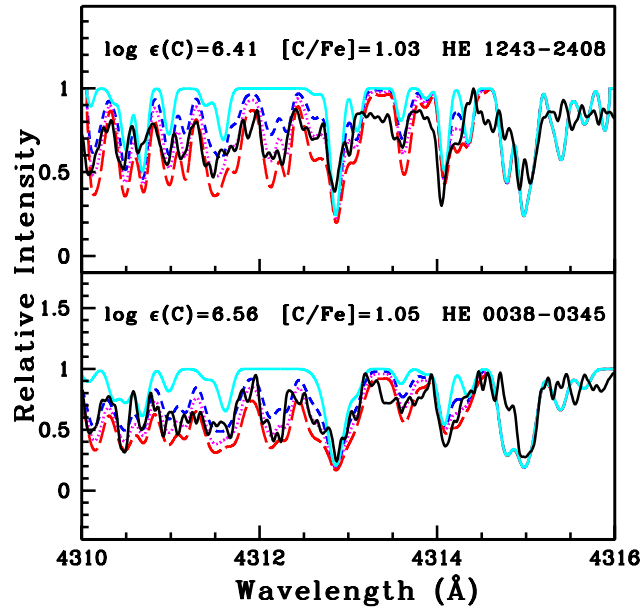

Figure 4. Spectrum synthesis fits of CH G-band around 4315 Å. Observed and synthetic spectra are represented by solid and dot lines, respectively. The synthetic spectra for Δ [C/Fe] = −0.3 and +0.3, respectively, are represented by short- and long-dashed lines. The cyan solid lines are the synthesized spectra without carbon.
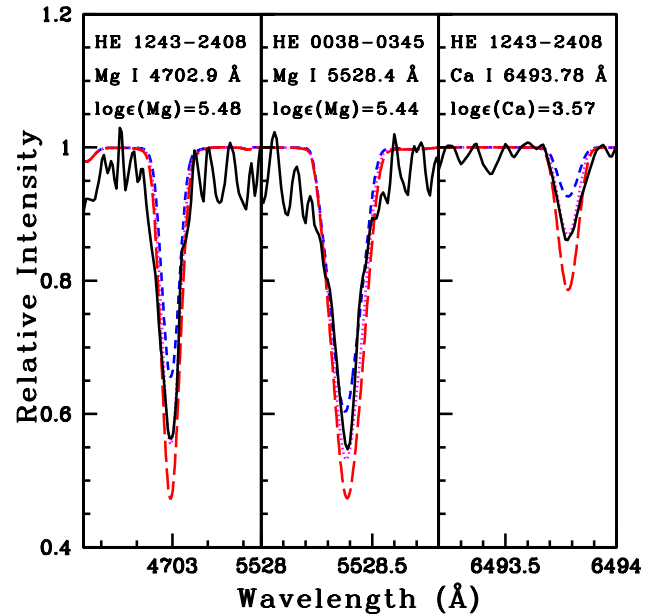

Figure 5. Spectrum synthesis fits for Mg I 4702.9, 5528.4 Å and Ca I 6493.78 Å lines. Observed and synthetic spectra are represented by solid and dot lines, respectively. The synthetic spectra for Δ [X/Fe] = −0.3 and +0.3, respectively, are represented by short- and long-dashed lines.

1243 − 2408, respectively. The spectral synthesis fits for the alpha elements Mg and Ca are shown in Fig. 5.

6.2 Heavy elements

We have derived the abundances of heavy elements Sr, Y, Zr, Ba, and Eu in our programme stars, whenever possible. The spectrum synthesis calculation is used for the abundance determination of all these elements. The Sr abundance could be determined only for HE 0038 − 0345 as there are no good lines of Sr detected in the spectra

of the other object. The abundance of Sr derived using the Sr II 4215.519 Å line is found to be under-abundant in this object with [Sr/Fe]~ -0.82. The yttrium abundance is derived from the Y II 5087.420 Å line in HE 0038 − 0345, and Y II 4883.684 Å line in HE 1243 − 2408. In the case of HE 0038 − 0345, we could only derive the upper limit to yttrium abundance. In both stars, yttrium is found to be under-abundant with values [Y/Fe]≤ -0.39. We could derive an upper limit to the Zr abundance in the object HE 1243 − 2408, where we have used Zr I 6134.999 Å line. Zirconium is found to be under-abundant in this object with [Zr/Fe]< -0.11. The abundance of barium is derived in both the programme stars. We have used Ba II 6141.7 Å line in HE 0038 − 0345, and Ba II 6496.9 Å line in HE 1243 − 2408. Ba is found to be under-abundant with values [Ba/Fe]$\sim$ -0.11 (HE 0038 − 0345) and -0.18 (HE 1243 − 2408). We have derived an upper limit to the Eu abundance in HE 0038 − 0345. The europium abundance is derived from the Eu II 6645.07 Å line which returned a value [Eu/Fe]< 0.58 for this object.

7 ABUNDANCE UNCERTAINTIES

The uncertainty in the elemental abundances are calculated using the procedure discussed in Shejeelammal et al. (2020). The uncertainty in the elemental abundances as a result of the uncertainties in the stellar atmospheric parameters are calculated using

$$\sigma_{log\epsilon}^2 = \sigma_{ran}^2 + \left(\frac{\partial log\epsilon}{\partial T}\right)^2 \sigma_{T_{eff}}^2 + \left(\frac{\partial log\epsilon}{\partial logg}\right)^2 \sigma_{logg}^2 + \left(\frac{\partial log\epsilon}{\partial \zeta}\right)^2 \sigma_\zeta^2$$
$$+ \left(\frac{\partial log\epsilon}{\partial [Fe/H]}\right)^2 \sigma_{[Fe/H]}^2$$

The uncertainties in the atmospheric parameters (σ's) are Δ(T$_{eff}$, log g, ζ, [Fe/H]) $\sim \pm$ (100 K, 0.2, 0.2 km s^{-1}, 0.1). The partial derivatives (∂) in the above equation are evaluated by changing the parameters by an amount equal to their respective uncertainties. The line-to-line scatter, standard deviation (σ_s), of the abundances of a specific element species determined from N number of lines gives rise to the random error in elemental abundance, which is calculated as $\sigma_{ran} = \frac{\sigma_s}{\sqrt{N}}$. The cumulative uncertainty on the abundance of an element (say X) is computed from

$$\sigma_{[X/Fe]}^2 = \sigma_X^2 + \sigma_{Fe}^2$$

The uncertainty on [X/Fe] of each element is calculated in the specific case of HE 0038 − 0345. Since Sc II and Zr I could not be detected in this object, we used HE 1243 − 2408 to calculate the uncertainty in the abundances of these two elements. Table 4 gives the calculated uncertainty on [X/Fe], $\sigma_{[X/Fe]}$, of each element.

8 ABUNDANCE ANALYSIS AND DISCUSSION

The two objects analysed in this study, HE 0038 − 0345 and HE 1243 − 2408, are found to be extremely metal-poor stars with [Fe/H]~ -3. The observed nitrogen abundances in them are [N/Fe] $<$ 2.92 (HE 0038 − 0345) and $<$ 3.55 (HE 1243 − 2408). The neutron-capture elements are found to be under abundant (< -0.1) in both the objects. The stars on the Red-Giant Branch (RGB) undergo internal mixing and hence alters the surface CN abundances (eg. Gratton et al. 2000; Spite et al. 2006; Aoki et al. 2007; Placco et al. 2014). Based on the analysis of a sample of 505 metal-poor ([Fe/H] ≤ -2) stars with no enhancement of neutron-capture elements from the literature, Placco et al. (2014) shown that the frequency of CEMP-no stars ([C/Fe] ≥ 0.7) in the galaxy is increased by $\sim$ 11 per cent for [Fe/H] ≤ -3, when proper correction required for the carbon depletion is applied to the observed [C/Fe].

Table 4. Variation in the abundances ($\Delta log\epsilon$) of various elements (of the star HE 0038 − 0345) with changes in each stellar atmospheric parameters (columns 2–5). Total uncertainty on [X/Fe] of each element is given in the last column.

Element	ΔT$_{eff}$ ($\pm$100 K)	Δlog g ($\pm$0.2 dex)	$\Delta\zeta$ ($\pm$0.2 km s^{-1})	Δ[Fe/H] ($\pm$0.1 dex)	$\sigma_{[X/Fe]}$
C	$\pm$0.20	$\mp$0.02	0.00	0.00	0.23
N	$\pm$0.30	$\mp$0.06	$\pm$0.02	0.00	0.32
Na I	$\pm$0.05	$\mp$0.01	0.00	0.00	0.12
Mg I	$\pm$0.06	$\mp$0.02	$\mp$0.02	0.00	0.15
Si I	$\pm$0.04	0.00	0.00	0.00	0.11
Ca I	$\pm$0.07	$\mp$0.02	$\mp$0.03	$\mp$0.01	0.14
Sc II	$\pm$0.05	$\pm$0.05	$\mp$0.03	$\mp$0.00	0.13
Ti I	$\pm$0.13	$\mp$0.02	$\mp$0.02	0.00	0.19
Ti II	$\pm$0.04	$\pm$0.07	$\mp$0.02	$\pm$0.01	0.14
Cr I	$\pm$0.13	$\mp$0.03	$\mp$0.08	$\mp$0.01	0.21
Fe I	$\pm$0.10	0.00	$\mp$0.01	0.00	–
Fe II	$\mp$0.03	$\pm$0.09	$\mp$0.01	$\pm$0.03	–
Ni I	$\pm$0.07	0.00	0.00	0.00	0.13
Zn I	$\pm$0.03	$\pm$0.03	$\mp$0.02	0.00	0.11
Sr II	$\pm$0.13	$\pm$0.05	$\mp$0.08	$\pm$0.02	0.19
Y II	$\pm$0.05	$\pm$0.06	$\mp$0.01	$\pm$0.01	0.13
Zr I	$\pm$0.06	0.00	$\mp$0.05	$\mp$0.02	0.13
Ba II	$\pm$0.07	$\pm$0.06	$\mp$0.04	$\pm$0.01	0.14
Eu II	$\pm$0.05	$\pm$0.07	$\mp$0.03	$\pm$0.01	0.14

Since both our programme stars are giants (Fig. 3 and Table 2), it is likely that the stars have undergone internal mixing, altering the surface CN composition (Spite et al. 2005; Placco et al. 2014). We have checked the [C/N] ratio, an indicator of mixing, of the programme stars as discussed in Spite et al. (2005). The plot of [C/N] ratio with respect to effective temperature of the programme stars is shown in Fig. 6. The [C/N] values of other known CEMP stars are also plotted in the same figure, for a comparison. From the figure, it is clear that both programme stars are mixed, with [C/N]< -0.6 (Spite et al. 2005). Since CEMP-no stars are important objects for studying the first stellar populations and the Initial Mass Function (IMF), the identification of genuine CEMP-no stars is crucial. Hence, we have applied the necessary evolutionary correction to the observed carbon abundance values in order to take account of any extra mixing on the giant branch that could have altered the carbon abundance. The corrections to the carbon abundances are calculated using the on-line tool publicly available at http://vplacco.pythonanywhere.com/, developed by Placco et al. (2014). The calculated correction factors are +0.13 and +0.46 for HE 0038 − 0345 and HE 1243 − 2408, respectively and the final corrected [C/Fe] values for them are 1.05 and 1.03. The observed and corrected [C/Fe] values of the programme stars, along with other CEMP stars from Placco et al. (2014) are plotted in Fig. 7. As we can see from this figure, for log g < 1.8, compared to CEMP-s and CEMP-r/s stars, a larger number of CEMP-no stars lie below [C/Fe] $\sim$ 0.7, even closer to [C/Fe] $\sim$ 0. The amount of carbon depleted are noticeably larger for lower surface gravities ($<$1.8), and all the stars in this region are brought to [C/Fe] $>$ 0.7 when corrected for the mixing. With the corrected [C/Fe] values ($>$1) and [Ba/Fe] values ($<$ 0), our programme stars are found to belong to CEMP-no classification (Beers & Christlieb 2005).

Since the programme stars are enhanced in nitrogen, we have examined if the stars are Nitrogen-Enhanced Metal-Poor (NEMP) star candidates. The NEMP stars are those with [N/Fe] $\geq$ 1 and [C/N] ≤ -0.5, according to Johnson et al. (2007). They generally show enhancement of s-process elements in addition to nitrogen and are mostly found at [Fe/H] < -2.9. Binary mass transfer from
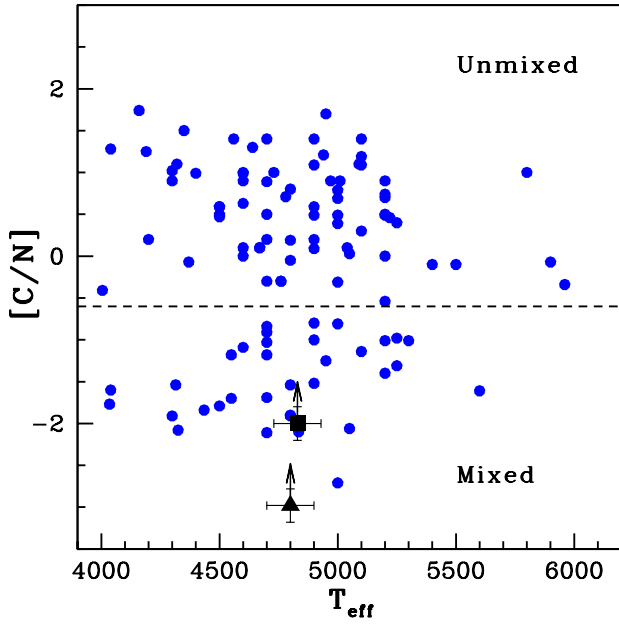
Figure 6. Distribution of [C/N] ratio as a function of T_{eff} for CEMP stars from the literature (Purandardas & Goswami 2021a and references therein, Goswami, Rathour & Goswami 2021; Shejeelammal & Goswami 2021; Shejeelammal, Goswami & Shi 2021; Shejeelammal & Goswami 2022). Our programme stars HE 0038 − 0345 (filled square) and HE 1243 − 2408 (filled triangle) are shown in black; these are the lower limits for the [C/N] ratio.
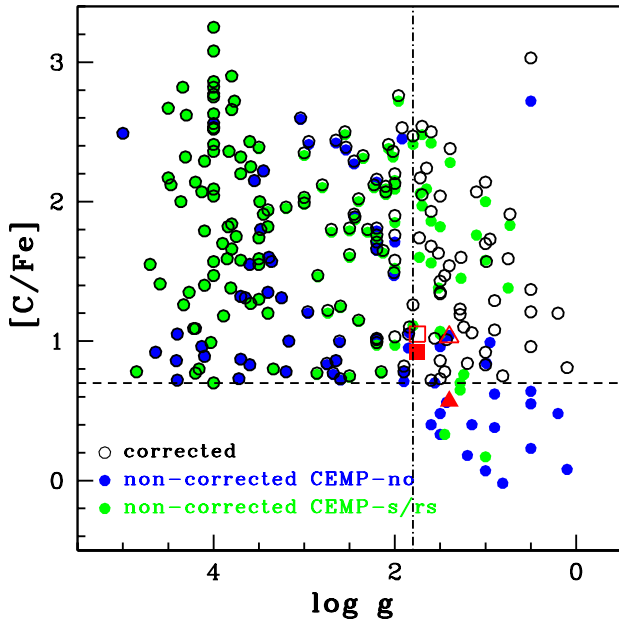

Figure 7. Distribution of [C/Fe] ratio as a function of log g for CEMP stars from the literature (Placco et al. 2014 and references therein). The observed [C/Fe] of the CEMP-no stars are shown with blue filled circles, and CEMP-s and CEMP-r/s stars with green filled circles. The corrected [C/Fe] abundance for the evolutionary effect are shown with black open circles. The red symbols represent our programme stars HE 0038 − 0345 (square), and HE 1243 − 2408 (triangle); where filled symbols are observed [C/Fe] and open symbols are corrected [C/Fe]. The dashed horizontal line corresponds to [C/Fe] = 0.7, and the vertical dot-dashed line corresponds to log g = 1.8.

intermediate-mass AGB stars with hot-bottom burning (HBB; M $\geq 5\,M_\odot$) are suggested to be the origin of these class of stars (Johnson et al. 2007; Pols et al. 2012; Simpson & Martell 2019). At lower metallicities (~ -2.3), the stars of lower masses ($\sim 3\,M_\odot$) could experience HBB, and hence the same mechanism that produce CEMP-s stars would produce NEMP stars as well (Johnson et al. 2007; Pols et al. 2012). However, they are rare and only ~ 15 NEMP stars were identified till date (Pols et al. 2012; Simpson & Martell 2019). Four out of these 15 objects show no evidence of s-element enhancement, similar to CEMP-no stars. According to Komiya et al. (2007), the binary mass transfer from low metallicity AGB stars ([Fe/H] < -2.5) with masses in the range 3.5–$6\,M_\odot$ could produce CEMP-no stars. In such a scenario, NEMP stars with no s-element enhancement are expected to be formed through the same process of mass-transfer that would produce CEMP-no stars (Pols et al. 2012). We found that the programme stars satisfy the conditions [N/Fe] ≥ 1 and [C/N] ≤ -0.5 to be NEMP stars. According to the definitions of CEMP and NEMP stars, they tend to overlap partially (some CEMP stars show [N/Fe] ≥ 1 and [C/N] ≤ -0.5), and the internal mixing on RGB could lead to the misinterpretation of CEMP stars as NEMP stars (Pols et al. 2012). In the study of Pols et al. (2012), among the 24 NEMP candidates identified according to the above definition, 10 objects are found to be internally mixed true CEMP stars on RGB. So, though the programme stars follow the definition of NEMP stars, based on the discussion in the previous paragraph and from Figs 6 and 7, we conclude that our objects are bonafide CEMP-no stars.

Detailed abundance profile analysis of the programme stars and the interpretation are presented in the following subsections.

8.1 Carbon abundances and location of the programme stars on the Yoon – Beers A(C) – [Fe/H] diagram

The identification and further studies on the existence of two carbon plateaus of CEMP stars in the distribution of absolute carbon abundance A(C) versus metallicity [Fe/H] point at the likelihood of different mechanisms for the production of carbon in CEMP stars (Spite et al. 2013; Bonifacio et al. 2015; Hansen et al. 2015; Yoon et al. 2016). According to the extended literature compilation performed by Yoon et al. 2016, the two plateaus are at carbon abundance values A(C)~7.96 and 6.28. Their analysis have further shown that different classes of CEMP stars exhibit different morphology on the A(C) – [Fe/H] diagram, and based on the morphology the stars are classified into three groups. In this plot, the high-carbon band is occupied by the CEMP-s and CEMP-r/s stars, with a wide scatter in A(C) at any given [Fe/H]. The stars in this band is referred as Group I stars. They show a very weak trend of A(C) with respect to [Fe/H]. The CEMP-no stars that occupy the low-carbon band exhibit two distinct behaviours. One subset ($-5 \leq$[Fe/H]≤ -2.5) shows a clear dependence of A(C) on [Fe/H], referred as Group II stars, and another sub-set with no clear dependence of A(C) on [Fe/H], referred as Group III stars. Different morphology of the three groups of CEMP stars led to the interpretation that these stars have different origin. The radial velocity studies of different CEMP stars have shown that stars in the low-carbon band (CEMP-no) are generally single stars and those in the high-carbon band (CEMP-s and CEMP-r/s) are generally binaries. Hence, binary mass-transfer from a companion AGB star is supported as the origin of CEMP-s and CEMP-r/s stars (Starkenburg et al. 2014; Bonifacio et al. 2015). The exact origin of CEMP-no stars has not been clearly understood yet, however, it is inferred that they are born from a natal cloud polluted by massive Pop III stars (Norris et al. 2013; Cooke & Madau 2014; Frebel & Norris 2015).
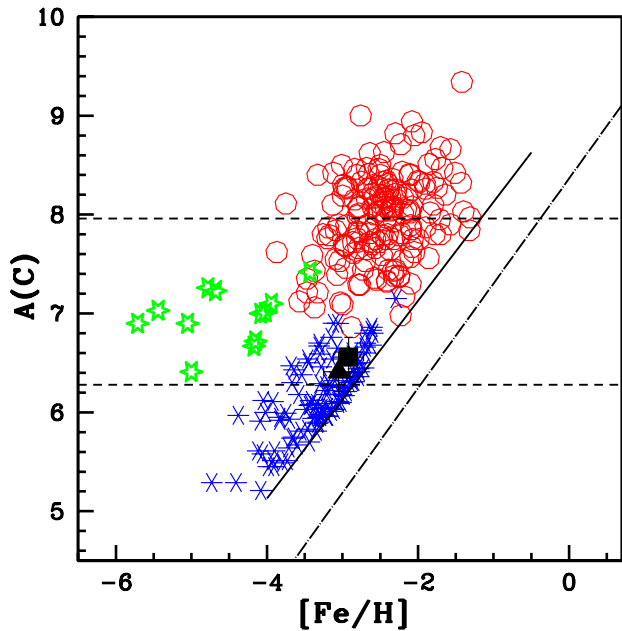
Figure 8. Distribution of A(C) as a function of [Fe/H] for CEMP stars from the literature (Yoon et al. 2016; Purandardas et al. 2019; Goswami, Rathour & Goswami 2021; Shejeelammal & Goswami 2021; Shejeelammal, Goswami & Shi 2021; Purandardas & Goswami 2021a, b; Shejeelammal & Goswami 2022). Red symbols are Group I CEMP stars. Blue and green symbols represent Group II and Group III CEMP-no stars, respectively. Our programme stars HE 0038 − 0345 (filled square), and HE 1243 − 2408 (filled triangle) are shown in black. The high- (A(C)∼7.96) and low- (A(C)∼6.28) carbon bands of CEMP stars are shown with dashed lines. The solid line is for [C/Fe] = 0.70 and long-dash dot line represent the solar carbon value, [C/Fe] = 0.

The locations of our programme stars on the A(C) – [Fe/H] diagram, along with other CEMP stars from the literature, are shown in the Fig. 8. The carbon abundances corrected for the evolutionary effect are used in this plot. As it is clear from the Fig. 8, the two programme stars fall in the region of Group II CEMP-no stars. Radial velocity studies of the programme stars are not available in the literature. However, our estimated radial velocities are similar to those listed in the *Gaia*. This may indicate that these stars are likely single, but not conclusively.

In the following sections we have discussed the possible progenitors of the programme stars based on a detailed analysis of their abundance patterns.

8.2 Analysis of abundance patterns observed in the programme stars and comparison with the literature

The observed abundances of different elements in the programme stars are compared with those in other CEMP-no stars and EMP stars from the literature. These comparisons are shown in Fig. 9. The estimated elemental abundances in the programme stars match closely with the abundances of elements in other extremely metal-poor stars. Both programme stars show enhancement of N, Na, and Mg. HE 0038 − 0345 show enhancement of Si as well, while Si abundance is not available for HE 1243 − 2408. These elements are found to be over abundant in majority of extremely metal-poor stars, indicating the signatures of first star nucleosynthesis (Aoki et al. 2002; Nomoto, Kobayashi & Tominaga 2013; Roederer et al. 2014; Aoki et al. 2018).
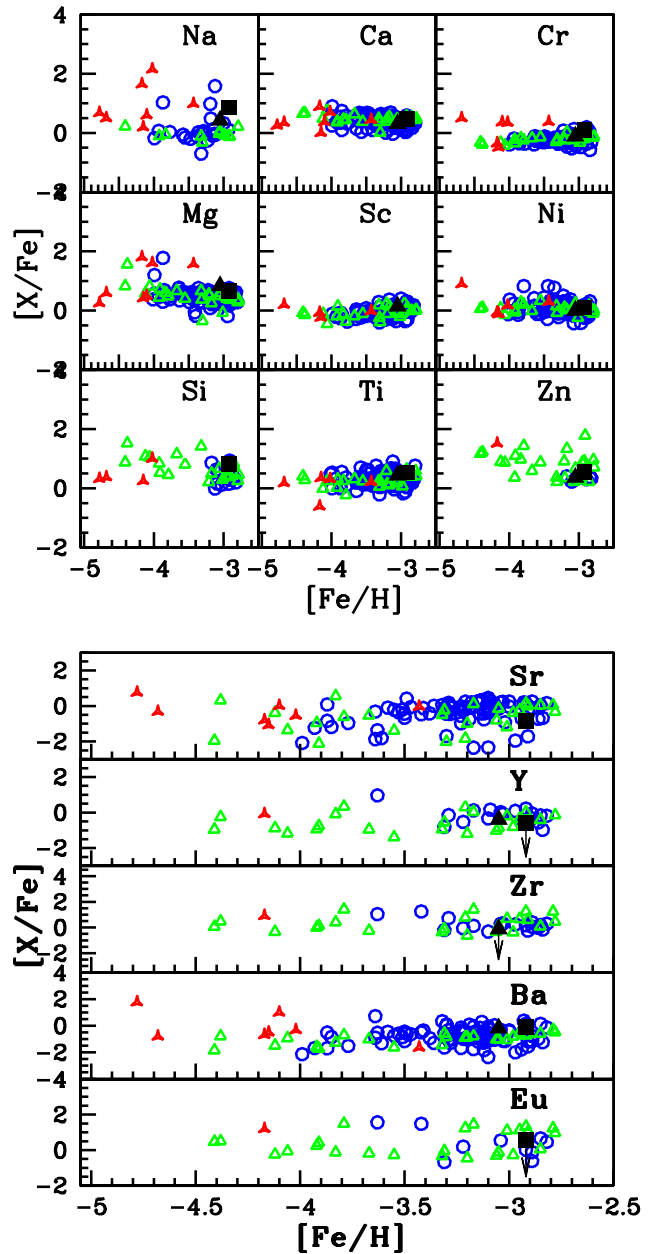

Figure 9. Observed [X/Fe] ratios of the light elements (upper panel) and heavy elements (lower panel) in the programme stars with respect to metallicity [Fe/H]. Green triangles and red starred triangles correspond to Group II and III CEMP-no stars, respectively from the literature (Yoon et al. 2016 and references therein, Purandardas & Goswami 2021a). Blue open circles represent extremely metal-poor stars from the literature (Honda et al. 2004; Venn et al. 2004; Aoki et al. 2005, 2007; Roederer et al. 2014). Our programme stars HE 0038 − 0345 (filled square), and HE 1243 − 2408 (filled triangle) are shown in black. The NLTE Na abundances are plotted for the programme stars. The symbols with downward arrow indicate the derived upper limit for the abundances.

A close match of the abundance ratios of the programme stars with their counterparts observed in the Group II CEMP-no stars (Fig. 9), indicates that the programme stars likely belong to the same group. The two groups of CEMP-no stars show distinct behaviours in terms of the abundances of Na, Mg, and Ba, in addition to carbon explained in the previous section. There exist a strong correlation

between A(C, Na, Mg, Ba) and [Fe/H] among Group II CEMP-no stars, where as there is no such dependence among the Group III CEMP-no stars (Yoon et al. 2016, 2019). We have examined the abundances of Na, Mg, and Ba, with respect to A(C) and [Fe/H] and performed a comparison with Group II and Group III CEMP-no stars from the literature. These plots are shown in Fig. 10. The locations of the programme stars in these plots suggest that they are Group II CEMP-no stars, similar to that inferred from Figs 8 and 9.

8.3 Possible origin of the programme stars

Origin of CEMP-no stars is still an open question with several suggested scenarios that include pre-enrichment of their natal cloud by faint SNe, spinstars, metal-free massive stars, or the contribution from all these sources (Yoon et al. 2016 and references therein, Hansen et al. 2016a). However, the study of Arentsen et al. (2019) shown that the binary fraction of CEMP-no stars is about 32 per cent (11 out of 34 stars), where eight of these stars have high-carbon abundance (A(C) > 6.6). This led them to suggest that at least a few of these stars might have been polluted by extremely metal-poor AGB stars that produced carbon but not a significant amount of s-process elements, like the abundances observed in these stars.

From the complex morphology of A(C)–[Fe/H] space for CEMP-no stars and their distinct behaviour in terms of abundances of Na and Mg, Yoon et al. (2016) presented the first evidence for the operation of at least two different classes of first-generation stellar progenitors for the CEMP-no stars. This hypothesis has been supported by Placco et al. (2016) from the analysis of 12 UMP CEMP-no stars. Likelihood of existence of multiple formation pathways for CEMP-no stars has been confirmed consequently by several other authors (Arentsen et al. 2019; Yoon et al. 2019, 2020; Dietz et al. 2021; Jeon et al. 2021; Purandardas & Goswami 2021a). It may also be possible that, a single yet to be identified process, could account for the abundance pattern of all UMP stars (Placco et al. 2016). Alternatively, more than one progenitors could also contribute to the observed abundance pattern of the same CEMP-no star (Placco et al. 2016; Arentsen et al. 2019; Yoon et al. 2019).

From the abundance characteristics of the two groups of CEMP-no stars, and previous studies on BD + 44 493 (Group II star) and HE 1327-2326 (Group III star), Yoon et al. (2016) had suggested that the progenitors of Group II stars may be faint SNe and that of Group III stars may be spinstars. Placco et al. (2016) performed an analysis to identify the progenitors of 12 UMP stars in their sample. They have considered the non-rotating, metal-free massive star models of Heger & Woosley (2010) for a mass range 10–100 $M_\odot$, and compared these yields with the light element abundance patterns of their sample. The abundance patterns of only 5 out of 12 stars could be reproduced with the SN models of Heger & Woosley (2010). Among these five stars, three objects are Group II stars, and the rest two are Group III stars.

In the context of a hierarchical Galactic assembly, Yoon et al. (2019) performed a comparison of the morphology of Galactic halo CEMP-no stars on the A(C)–[Fe/H] diagram with those of CEMP-no stars in the dwarf satellite galaxies – ultra-faint Dwarfs (UFDs) and dwarf spheroidal (dSph) galaxies, of the Milky Way (MW). A very similar behaviour of A(C)–[Fe/H] as that of halo stars, with two distinct groups, is found among the CEMP-no stars of the UFD and dSph galaxies. This similarity in the morphology among these stars is a strong evidence that CEMP-no halo stars are accreted from the mini-halos, supporting various studies of Galactic assembly and halo formation (Frebel & Norris 2015; Amorisco 2017; Starkenburg et al. 2017; Spite et al. 2018). The characteristics of each group of CEMP-
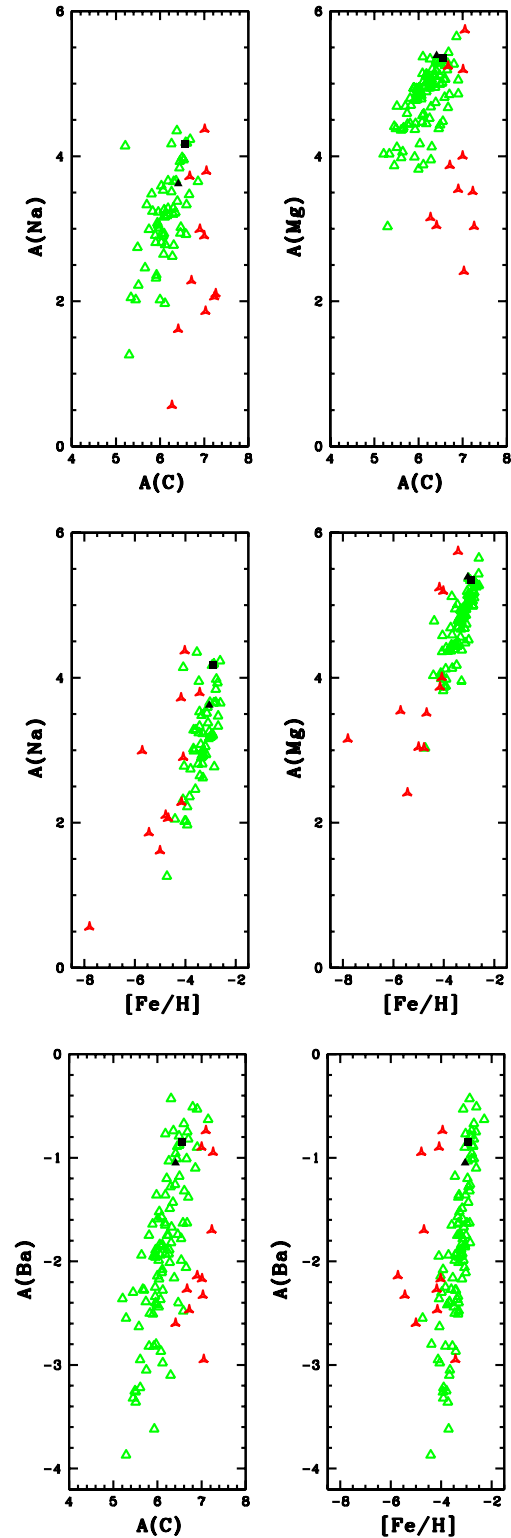

Figure 10. Observed A(Na), A(Mg), and A(Ba) values with respect to A(C) and metallicity [Fe/H]. Symbols have same meaning as in Fig. 9.

no stars depend on the nature of the host mini-halos. While the UFD galaxies host both Group II and III stars, the dSph galaxies host only Group II stars, due to several distinct properties of these galaxies such as mass, star formation history (SFH), metal-enrichment/pollution pathways, cooling agents, etc (Yoon et al. 2018, 2019, 2020 and references therein). According to the study by Yoon et al. (2019), the majority of Group II CEMP-no stars in the Galactic halo are likely accreted from dSph-like systems, and the Group III CEMP-no stars are likely accreted from UFD-like satellite galaxies.

The dSphs are massive ($\geq 10^9 \, \mathrm{M_\odot}$) with more gas content than UFDs that result in extended star formation, leading to the formation of Pop II stars that explode as core collapse supernovae, in addition to the Pop III supernovae. This results in a more metal-rich environment. The extended SFH leading to the strong chemical evolution is reflected as strong correlation among A(C), A(Na, Mg, Ba), and [Fe/H]. The next generation stars are formed from the well-mixed ISM enriched by multiple SNe, both from Pop II and III (Salvadori, Skúladóttir & Tolstoy 2015; de Bennassuti et al. 2017; Chiaki, Susa & Hirano 2018).

In contrast, UFDs are less massive ($\leq 10^6 \, \mathrm{M_\odot}$) with dark-matter dominated halos. These mini-halos likely undergo only one or a few generations of star formation due to low star formation efficiency and supernovae feed back (Salvadori & Ferrara 2009; Vincenzo et al. 2014; Jeon, Besla & Bromm 2017). As a result, the stars in these systems are primitive and likely mono-enriched, as evident from their low metallicity and [Mg/C] value (<-0.5) (Hartwig et al. 2018). Only one Pop III progenitor – CCSNe, faint SNe, and/or spinstars, had enriched the natal clouds of these Group II and Group III stars (Salvadori, Skúladóttir & Tolstoy 2015; de Bennassuti et al. 2017).

The distinct abundance patterns of Group II and Group III stars support these different formation environments. The abundances of elements C, Na, Mg, and Fe suggest that Group II stars are likely formed from the gas cooled by the silicate grains, whose key elements are Mg and Si that are main products of CCSNe. The Group III stars are formed from the gas cooled by the carbon grains, whose key element is carbon, which is mainly produced by spinstars and/or faint SNe (Chiaki, Tominaga & Nozawa 2017, Yoon et al. 2019, 2020 and references therein). The simulations of Jeon et al. (2021) have shown that the Group II CEMP-no stars attribute their origin to normal SNe and Group III CEMP-no stars to faint SNe.

We have found from the abundance analysis, as discussed in the previous sections, that our programme stars belong to Group II CEMP-no stars. We have examined the [Mg/C] ratio of the programme stars to see if they are mono-enriched or multi-enriched. According to Hartwig et al. (2018), the stars with [Mg/C]<-1 are mono-enriched. It should be noted that, like carbon, the abundances of the light elements Li, Mg, and Fe are found to show significant changes in metal-poor stars as they evolve from the turn-off point to RGB, owing to atomic diffusion. In the case of Mg and Fe, the corrections can be as much as -0.3 dex; however, it has very little impact on [X/Fe] ratio of these elements (Korn et al. 2007). We have applied the diffusion correction of -0.3 to the [Mg/H] values of the programme stars before calculating [Mg/C] ratio. The calculated (diffusion corrected) values of this ratio in HE 0038 $-$ 0345 and HE 1243 $-$ 2408, respectively are -0.68 and -0.49, indicating multi-enrichment. The location of the programme stars on the [Mg/C] $-$ [Fe/H] plot is shown in Fig. 11, along with other CEMP-no stars from the literature. The programme stars are found to be multi-enriched based on the [Ca/Fe] value (<2) as well. If the result of Yoon et al. (2019) holds true, this multi-enrichment suggests that the programme stars may owe their origin to the dSph satellite galaxies, as discussed above. Further, they might have formed from
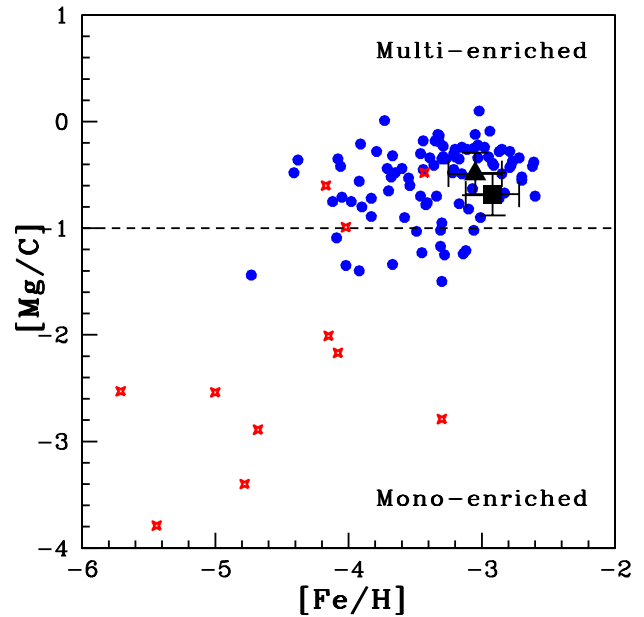

Figure 11. Distribution of [Mg/C] as a function of [Fe/H] for CEMP-no stars. Blue circles are Group II CEMP-no stars and red stars are Group III CEMP-no stars from the literature (Purandardas & Goswami 2021b and references therein). Our programme stars HE 0038 $-$ 0345 (filled square), and HE 1243 $-$ 2408 (filled triangle) are shown in black.

the gas cloud pre-enriched by CCSNe, from the ground of arguments discussed previously in this section. In the case of spinstar progenitor, the stars are expected to show [Sr/Ba]>0 (Frischknecht, Hirschi & Thielemann 2012; Hansen et al. 2019). We could estimate this ratio in the object HE 0038 $-$ 0345, it returned a value [Sr/Ba]~ -0.71, discarding spinstar progenitor. In the case of faint SNe progenitor, the stars are expected to show [C/Fe]≥ 2. The faint SNe are found to contribute in the metallicity range $-5.5 \leq$[Fe/H]≤ -3.5. In the case of stars with [C/Fe]<1 and $-4 \leq$[Fe/H]≤ -3, CCSNe are found to contribute to the abundance pattern (Umeda & Nomoto 2003, 2005; Tominaga, Iwamoto & Nomoto 2014; Mardini et al. 2022). Further, the CEMP-no stars with [C/Fe]≥ 2 are originated from Pop III stars, and Pop II stars are responsible for the origin of CEMP stars with [C/Fe]< 2 (Jeon, Besla & Bromm 2017; Jeon et al. 2021). Hence, from the [C/Fe] values (<2) and [Fe/H] (~ -3), the progenitors of our programme stars are likely Pop II CCSNe.

We have compared the abundances of the programme stars with those in the CEMP-no stars of the dSPhs and UFDs from the literature (SAGA data base; http://sagadata base.jp/). This comparison is shown in Fig. 12. From the figure, it is obvious that the abundance pattern of Group II CEMP-no stars of the galaxy matches with those in the dSphs. As seen from the Fig. 11, majority of Group II CEMP-no stars are multi-enriched, reinforcing their origin in dSphs. Also, the elemental abundances of the programme stars match closely with those in the CEMP-no stars of the dSphs. From this, along with the observations discussed earlier in this section, we infer that our programme stars are likely accreted from the dSph satellite galaxies.

In the next section, we have discussed the accretion origin of the programme stars on the ground of kinematic analysis.

9 KINEMATIC ANALYSIS

The components of spatial velocity, total spatial velocity, and the Galactic population of the programme stars are estimated following
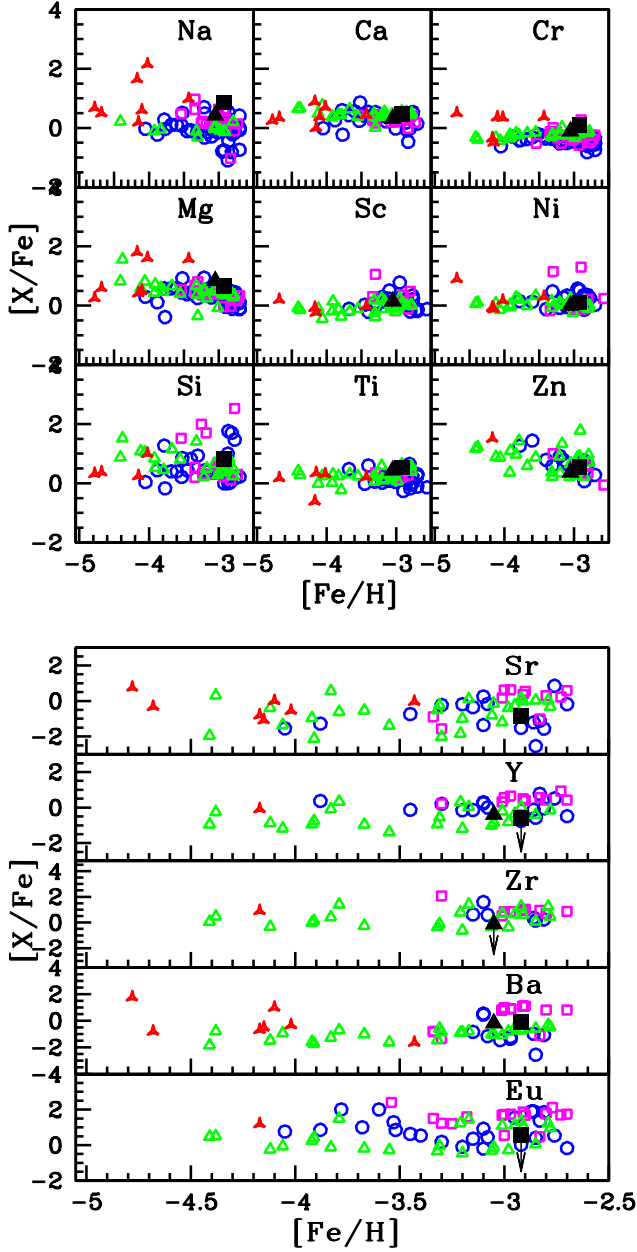
Figure 12. Observed [X/Fe] ratios of the light elements (upper panel) and heavy elements (lower panel) in the programme stars with respect to metallicity [Fe/H]. The blue open circles represent the CEMP-no stars in the dSph satellite galaxies and magenta open squares are the CEMP-no stars in the UFD satellite galaxies from the literature (http://sagadatabase.jp/). Other symbols have same meaning as in Fig. 9. Our programme stars HE 0038 − 0345 (filled square), and HE 1243 − 2408 (filled triangle) are shown in black. The symbols with downward arrow indicate the derived upper limit for the abundances.

the procedures described in Johnson & Soderblom (1987), Bensby, Feltzing & Lundström (2003, 2004), Mishenina et al. (2004), and Reddy, Lambert & Allende Prieto (2006). The detailed procedure is discussed in our previous paper Shejeelammal, Goswami & Shi (2021).

The components of spatial velocity with respect to the Local Standard of Rest (LSR) is calculated as

$$(U, V, W)_{LSR} = (U, V, W) + (U, V, W)_\odot \, \text{km s}^{-1}.$$

$(U, V, W)_\odot = (11.1, 12.2, 7.3) \, \text{km s}^{-1}$ is the solar motion with respect to LSR (Schönrich, Binney & Dehnen 2010).

Total space velocity with respect to LSR is estimated using

$$V_{spa}^2 = U_{LSR}^2 + V_{LSR}^2 + W_{LSR}^2.$$

The proper motions in RA (μ_α) and Dec. (μ_δ), and the parallax (π) values are taken from SIMBAD astronomical data base and *Gaia* DR3 (*Gaia* Collaboration et al. 2016; Babusiaux et al. 2022; *Gaia* Collaboration et al. 2022, https://gea.esac.esa.int/archive/).

The estimated spatial velocities, along with the probabilities of the objects to belong to the Galactic thin/thick disc and halo, are presented in Table 5. While the object HE 0038 − 0345 is found to belong to the thick disc with a probability of 0.82, the object HE 0038 − 0345 is found to be a member of the halo with a probability of 1. However, according to Koppelman, Helmi & Veljanoski (2018), the stars with $V_{spa} > 210 \, \text{km s}^{-1}$ are bonafide halo objects. Both our programme stars have total spatial velocities greater than this value (Table 5). If we follow this criterion, both the programme stars belong to the Galactic halo. A Toomre diagram (P_{LSR} vs V_{LSR}) demonstrating the location of the programme stars in the galaxy is shown in Fig. 13. In this plot, the $P_{LSR} = \sqrt{U_{LSR}^2 + W_{LSR}^2}$ is the perpendicular component of V_{LSR}. As seen from the figure, the object HE 0038 − 0345 lies marginally in the disc (with the lower limit), while HE 1243 − 2408 is a bonafide halo object. We have also calculated the spatial velocities of the stars from Hansen et al. (2019), and the MW satellite galaxies. These are also shown in Fig. 13, for a comparison. Here, we have included only the kinematically selected halo stars ($V_{spa} > 210 \, \text{km s}^{-1}$) from Hansen et al. (2019). We note that, a few satellite galaxies have velocities typical of the Galactic disc.

9.1 Orbital properties

We have computed the orbital characteristics of the programme stars to understand more about their origin. The orbital properties such as Galactocentric distances, Galactocentric velocities, angular momenta, orbital energies, are estimated using the galpy (http://github.com/jobovy/galpy, Bovy 2015) python package for Galactic dynamics. We used the high-precision astrometric data α, δ, μ_α, μ_δ, distance, and V_r, from *Gaia* DR3 (*Gaia* Collaboration et al. 2022) listed in Tables 1 and 6. We set the Galactocentric distance of the sun at $r_o = 8 \, \text{kpc}$, velocity at this distance at $V_o = 220 \, \text{km s}^{-1}$ (Bovy et al. 2012), and the vertical distance of the sun above the plane at $z_o = 20.8 \, \text{pc}$ (Bennett & Bovy 2019). The adopted solar motion with respect to LSR is $(U, V, W)_\odot = (11.1, 12.2, 7.3) \, \text{km s}^{-1}$ (Schönrich, Binney & Dehnen 2010).

Using these parameters as initial conditions, we have integrated the orbits 12 Gyr backwards in a Milky Way-like potential. In the default MWPotential2014 (Bovy 2015) in galpy, the bulge is parametrized by a power-law density profile that exponentially cut-off at 1.9 kpc with an exponent −1.8, the disc by Miyamoto–Nagai potential with vertical scale height of 280 pc and radial scale-length of 3 kpc (Miyamoto & Nagai 1975), and halo by Navarro–Frenk–White (NFW) potential with a scale-length of 16 kpc (Navarro, Frenk & White 1996). This potential is characterized by a virial radius, $r_{vir} = 245 \, \text{kpc}$ and a virial mass, $M_{vir} = 0.8 \times 10^{12} \, M_\odot$. However, according to recent studies based on the *Gaia* proper motions, the virial mass of the galaxy ranges from 1.1×10^{12} to $1.5 \times 10^{12} \, M_\odot$ (e.g. Watkins et al. 2019; Wang et al. 2020). The lower mass of the halo in the default MWPotential2014 lead to the inaccurate estimations of orbital parameters for Galactic halo objects, especially the orbital energies are highly over-estimated (Kim, Lee & Beers

Table 5. Estimated spatial velocity and probabilities of membership to the Galactic population of the programme stars.

Star name	U_{LSR} (km s^{-1})	V_{LSR} (km s^{-1})	W_{LSR} (km s^{-1})	P_{LSR} (km s^{-1})	V_{spa} (km s^{-1})	P_{thin}	P_{thick}	P_{halo}
HE 0038 − 0345	−199.22 ± 15.07	−41.72 ± 2.70	74.15 ± 2.07	212.57 ± 15.19	216.63 ± 13.54	0.00	0.82	0.18
HE 1243 − 2408	−6.01 ± 1.89	−390.06 ± 4.70	−72.57 ± 3.85	72.81 ± 4.28	396.80 ± 5.37	0.00	0.00	1.00
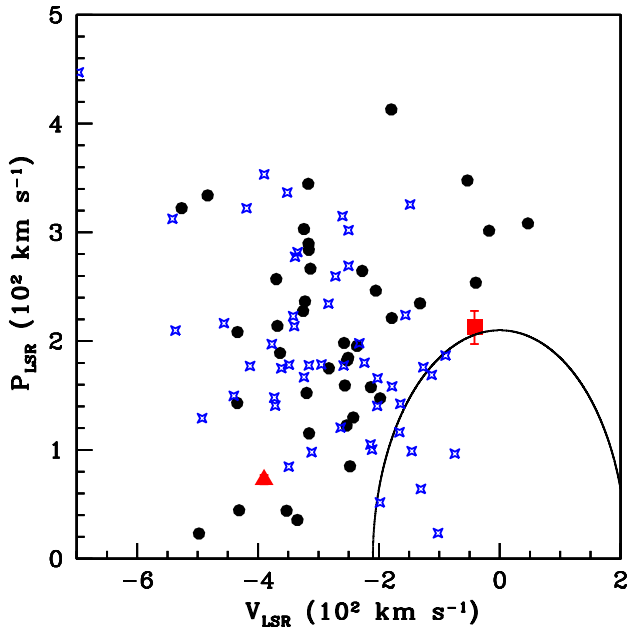
Figure 13. The Toomre diagram for the programme stars, HE 0038 − 0345 (filled square) and HE 1243 − 2408 (filled triangle). The black curve represents the loci of all points with $V_{spa} = 210$ km s^{-1}, separating halo and disc objects (Koppelman, Helmi & Veljanoski 2018). The black filled circles are kinematically selected halo stars from the literature (Hansen et al. 2019 and references therein). Blue stars represent the dwarf satellite galaxies of the MW.

2019; Woody & Schlaufman 2021). Kim, Lee & Beers (2019) noted that, many high-energy, retrograde stars in the outer halo are unbound in the default MWPotential2014. Hence, in our analysis, we have used a scaled version of the default MWPotential2014, where the halo mass is increased by 50 per cent. In the scaled

MWPotential2014, $M_{vir} \sim 1.2 \times 10^{12}\, M_{\odot}$, in agreement with the recent observations.

The computed orbital parameters – apocentric distance (r_{apo}), pericentric distance (r_{peri}), maximum height from the Galactic plane (z_{max}), eccentricity (e), total orbital energy (E_{tot}), components of angular momentum (L_x, L_y, L_z), Galactocentric tangential velocity (v_{ϕ}), and 3D Galactocentric distance, of the programme stars are given in Table 6. For a comparison purpose, we have calculated these parameters for the halo stars that were kinematically chosen from Hansen et al. (2019), as well as for the 50 MW satellite galaxies, using the same procedure and potential as the programme stars. The resulting parameters are shown in Figs 14 and 15, however, we have excluded the unbound (E_{tot} > 0) objects. In the Lindblad diagram (E_{tot} − L_z; Fig. 15), the star LAMOSTJ045019.27 + 394758.7, a sculptor dwarf galaxy escapee from the literature (Purandardas et al. 2022), is also shown.

We note from Fig. 15 that our programme stars and the escapee star LAMOSTJ045019.27 + 394758.7 have energies on par with a few satellite galaxies. The programme stars and the halo stars have similar orbital parameters, as seen in Fig. 14. We note that, in contrast to halo stars and programme stars, satellite galaxies exhibit greater r_{apo}, r_{peri}, and z_{max} values, yet all three samples' orbital eccentricities fall within the same range.

From Fig. 15, we can see that both our programme stars are bound to the galaxy (E_{tot} < 0), and belong to the high-energy (> −1.1 × 10^5 km^2 s^{-2}, Myeong et al. 2019) region. The object HE 0038 − 0345 has a prograde (L_z, v_{ϕ} > 0) orbit, whereas the object HE1243 − 2408 has a retrograde (L_z, v_{ϕ} < 0) motion. While HE 0038 − 0345 belongs to the outer halo (outer halo starts from $r_{apo} \sim 15$ − 20 kpc, Carollo et al. 2007) with $r_{apo} \sim 16.27$ kpc, HE 1243 − 2408 belongs to the inner halo (6 ≤ r_{apo} ≤ 13 kpc, Roederer et al. 2018) with $r_{apo} \sim 7.70$ kpc. To sum up, the star HE 0038 − 0345 is found to be a high-energy, prograde, outer halo object, and HE 1243 − 2408 is found to be a high-energy, retrograde, inner halo object.

Table 6. Galactic orbital parameters of the programme stars computed using galpy in a scaled MWPotential2014.

	HE 0038 − 0345	HE 1243 − 2408
Astrometric data from *Gaia* DR3:		
Galactic longitude, l (degrees)	116.56	301.32
Galactic latitude, b (degrees)	−66.23	+38.44
Proper motions, (μ_{α}, μ_{δ}) (mas yr^{-1})	(19.26, 8.46)	(−51.21, −58.59)
parallax, π (mas)	0.45	1.05
Radial velocity, V_r (km s^{-1})	−42.66	213.35
3D Galactocentric distance, r_{gal} (kpc)	8.69	7.67
Apocentric distance, r_{apo} (kpc)	16.27	7.70
Pericentric distance, r_{peri} (kpc)	4.25	4.60
Maximum height from the Galactic plane, z_{max} (kpc)	8.65	1.99
Orbital eccentricity, e	0.59	0.25
Total orbital energy, E_{tot} (10^5 km^2 s^{-2})	−0.69	−0.99
Angular momentum, (L_x, L_y, L_z) (10^3 kpc km s^{-1})	(0.42, −1.03, 1.34)	(0.15, 0.55, − 1.30)
Galactocentric tangential velocity, v_{ϕ} (km s^{-1})	158.70	−169.74

Table 7. Chemodynamical properties of MW substructures relevant to this study[†].

	In situ halo	I'itoi	*Gaia*-Sausage-Enceladus (GSE)	Sagittarius (Sgr)
E_{tot} (10^5 km^2 s^{-2})	< -0.8	> -1.25	< -0.5	$\sim -0.9 - -0.4$
L_z (10^3 kpc km s^{-1})	> 1.0	< -0.7	$\sim -150 - +150$	> 0
v_ϕ (km s^{-1})	> 200	< -100	$\sim -150 - +200$	> 50
Eccentricity, e	< 0.3	$0.1 - 0.7$	> 0.7	$\sim 0.4 - 0.7$
r_{gal} (kpc)	≤ 25	≤ 40	$\leq 50^{\ddagger}$	> 8
Metallicty, [Fe/H]*	> -1	< -2	~ -1.3	~ -1.0
[α/Fe]	$> 0.25 - 0.5$	$0.2 - 0.6$	$\sim 0.3 - 0.6^{\star}$	$\sim 0.4 - 0.6^{\star}$
L_y (10^3 kpc km s^{-1})	–	–	–	$< -0.3L_z - 2.5$

Notes.[†] Adopted from Naidu et al. (2020)
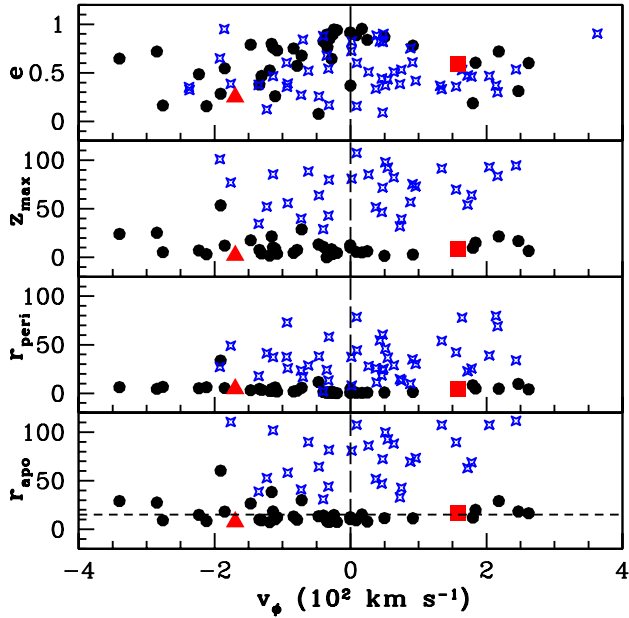[‡] The sample is limited up to 50 kpc; * Peak of MDF; * At [Fe/H]~ -3.0

Figure 14. The computed orbital parameters, v_ϕ, r_{apo}, r_{peri}, z_{max}, and eccentricity, for the same objects as in Fig. 13. The Y-axes of the bottom three panels are in kpc. The horizontal short-dashed line in the bottom panel represents the apocentric distance ($r_{apo} \sim 15$ kpc, Carollo et al. 2007) that separates outer halo from the inner halo. The vertical long-dashed line at $v_\phi = 0$ separates retrograde ($v_\phi < 0$) and prograde objects ($v_\phi > 0$). HE 0038 − 0345 (filled square) and HE 1243 − 2408 (filled triangle).

Figure 15. The Lindblad diagram for the same objects as in Fig. 13. The Y-axis is the total orbital energy in 10^5 km^2 s^{-2} ($E_{tot,5}$). The horizontal short-dashed line represents the high-energy limit $E_{tot} = -1.1 \times 10^5$ km^2 s^{-2} (Myeong et al. 2019). The vertical long-dashed line at $L_z = 0$ separates retrograde ($L_z < 0$) and prograde objects ($L_z > 0$). HE 0038 − 0345 (filled square) and HE 1243 − 2408 (filled triangle). The filled red circle is LAMOSTJ045019.27 + 394758.7, a sculptor dwarf galaxy escapee from the literature (Purandardas et al. 2022).

10 ASSOCIATION OF PROGRAMME STARS TO RECOGNIZED MILKY WAY STRUCTURES

The likelihood of accretion origin of the stellar halo with higher apocentres and/or retrograde orbits have been discussed by several authors (Roederer et al. 2018; Myeong et al. 2019; Dietz et al. 2020; Aguado et al. 2021). The chemodynamical analysis of samples of globular clusters, stars, stellar streams, satellite galaxies etc., have shown that the Galactic halo shows different substructures in the energy – action space ($E_{tot} - J_\phi$; $J_\phi \equiv L_z$), owing to various major and minor accretion events in the past (Myeong et al. 2019; Helmi 2020; Naidu et al. 2020; Aguado et al. 2021; Dietz et al. 2021; Woody & Schlaufman 2021; Malhan et al. 2022; Zepeda et al. 2023). In addition to the substructures associated with the major massive accretion events such as *Gaia*-Sausage-Enceladus (GSE), Kraken, and sequoia, several other structures such as LMS-1/Wukong, Thamnos, Metal-weak Thick Disc (MWTD), I'itoi, Splashed Disc (SD), Sagittarius
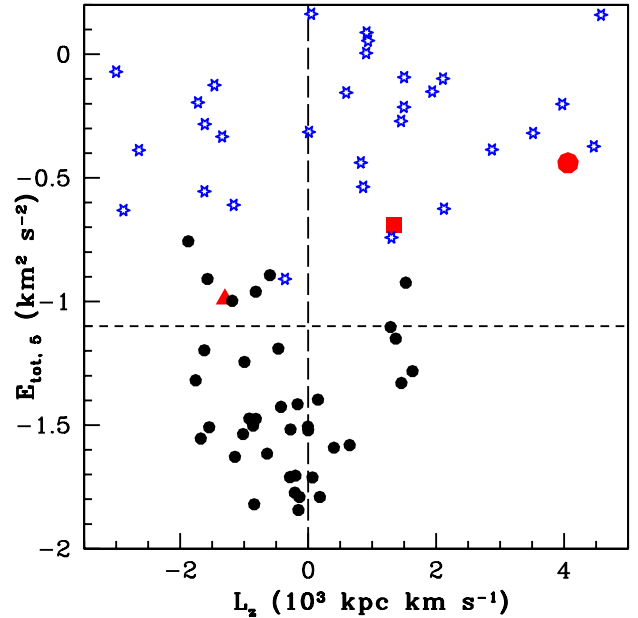
(Sgr), *in situ* Halo, Arjuna, Aleph, Helmi Streams etc. associated with minor mergers (massive/low-mass) are found to contribute significantly to the hierarchical Galactic halo assembly (Helmi et al. 2018; Helmi 2020; Naidu et al. 2020; Malhan et al. 2022; Naidu et al. 2022; Zepeda et al. 2023). Each of these substructures show different chemical and dynamical properties. Zepeda et al. (2023) grouped a sample of 644 CEMP stars to different Chemodynamically Tagged Groups (CDTGs) from their chemical abundances and orbital properties, and associated these CTDGs to various aforementioned Milky Way substructures.

We have performed a chemodynamical analysis of our programme stars, and compared their properties with those of Milky Way substructures to see if they could be associated with any of these accretion events. The properties of the MW structures relevant to this study are listed in Table 7. We found that none of our object meet the criteria of *in situ* halo (Table 7), and hence they belong

to the ex situ halo component. According to Dietz et al. (2020), while the high-energy, retrograde, outer halo, metal-poor objects are donated by the Sequoia dwarf progenitor galaxy, the EMP ([FeH]<-2), high-energy, prograde, outer halo objects are accreted onto the halo from a series of minor mergers. Recent studies have shown that the high-energy, retrograde halo is associated with Arjuna, Sequoia, and I'itoi events, depending on the metallicity (Naidu et al. 2020; Malhan et al. 2022).[1] The MDF of this component of halo has shown that the stars with [Fe/H]>-1.5 belong to Arjuna, those with $-2<$[Fe/H]<-1.5 to Sequoia, and with [Fe/H]<-2 to I'itoi structures. I'itoi, alternatively, might be thought of as a metal-poor tail of Sequoia and/or Arjuna (Naidu et al. 2020). We found from our inspection that our high-energy, retrograde object HE 1243 − 2408 satisfies the orbital as well as the chemical properties ([Fe/H], [α/Fe][2]) of the I'itoi substructure.

Our high-energy, prograde object HE 0038 − 0345 does not fully satisfy the requirement of any specific MW structure; it falls under the unclassified debris class of Naidu et al. (2020). However, they found that certain classes of this unclassified debris clustered around the selection boxes of various structures. These stars may be plausible members of that particular structure in whose close proximity they tend to cluster. If we consider such a scenario, the object HE 0038 − 0345 may plausibly belong to either the Sagittarius or the GSE. We note that even though the MDF of the GSE and the Sgr peaks at higher metallicities ([Fe/H]~-1.3 and -1.0, respectively; Myeong et al. 2018; Dietz et al. 2020; Naidu et al. 2020), they could contribute a few stars at metallicities as low as -3 (Zepeda et al. 2023, figs 8 and 11 of Naidu et al. 2020). The star HE 0038 − 0345 satisfies all the properties of the Sgr except for $L_y < -0.3L_z - 2.5$. Alternatively, it satisfies all the properties of the GSE structure except for the eccentricity (e$>$0.7); but with an estimated eccentricity of $\sim$0.6, this may be a possible member of the GSE as well.

Finally, we wind up this section with a discussion on the mass of the possible progenitor galaxies of the programme stars. From the above discussion, we infer the likely association of our programme stars with structures such as I'itoi, metal-poor extension of Arjuna/Sequoia (Arjuna may be a highly retrograde extension of GSE itself, as noted by Naidu et al. 2020), Sgr, or GSE. The progenitor satellite galaxies of all these events have stellar masses $M_\star \geq 10^8 - 10^9 \, M_\odot$ (Myeong et al. 2019; Kruijssen et al. 2020; Naidu et al. 2020, 2022). This mass of the progenitor galaxies is in agreement with the typical masses of dSphs, and hence this may justify the origin of programme stars in massive ($\geq 10^9 \, M_\odot$) dSph galaxies as discussed in subsection 8.3.

11 CONCLUSIONS

The high-resolution spectroscopic analysis of two CEMP star candidates, HE 0038 − 0345 and HE 1243 − 2408, selected from the HES is carried out. We present the first-time detailed chemodynamical analysis of these stars. Both the objects are found to be extremely metal-poor stars with [Fe/H]~-3.0. The estimated [C/Fe] values, 1.05 and 1.03 (after applying the correction), and [Ba/Fe] values, -0.11 and -0.18, for HE 0038 − 0345 and HE 1243 − 2408, respectively, show that both the objects are CEMP-no stars. From

the estimated [C/N] values, the stars are found to have undergone mixing that altered the surface carbon abundances.

The location of the programme stars on the A(C) – [Fe/H] diagram shows that both the objects belong to the Group II CEMP-no stars of Yoon et al. (2016). The observed abundances of Na, Mg, and Ba also confirms the assignment of the programme stars to the Group II. The [Mg/C] and [Ca/Fe] ratios of the objects reveal that they are multi-enriched. Based on the multi-enrichment and other abundance profile analysis, we found that the programme stars may have formed in the dSph satellite galaxies. This result is in strong agreement with the Galactic assembly and accretion of halo CEMP-no stars from mini-halos, as suggested by Yoon et al. (2018), Yoon et al. (2019), and Yoon et al. (2020). Furthermore, from the finding that the programme stars were likely born in the dSph-like systems, and based on the [C/Fe], [Fe/H], and [Sr/Ba] values, we found that the likely progenitors of the programme stars are Pop II core-collapse SNe.

We have performed a detailed kinematic analysis and derived various orbital and dynamical properties of the programme stars to derive non-abundance-based conclusions about their origin. The kinematic analysis shows that the objects HE 0038 − 0345 and HE 1243 − 2408 are members of the Galactic halo with $V_{spa}>210$ km s^{-1}. From the dynamical and orbital parameters, the object HE 0038 − 0345 is found to be a high-energy, prograde, outer halo object, and HE 1243 − 2408 is found to be a high-energy, retrograde, inner halo object. Our detailed chemodynamical analysis shows that HE 1243 − 2408 belongs to the I'itoi structure (which can be likely a metal-poor tail of the Sequoia and/or Arjuna), where as HE 0038 − 0345 is a plausible member of the Sgr or the GSE accretion events. The mass of the progenitor galaxies of the programme stars inferred from their dynamics ($M_\star \geq 10^8 - 10^9 \, M_\odot$), agrees with our speculations based on the chemical abundances that the stars may have originated in massive ($\geq 10^9 \, M_\odot$) dSph like systems.

12 DATA AVAILABILITY STATEMENT

The data underlying this article will be shared on reasonable request to the authors.

REFERENCES

---

[1]Naidu et al. 2020 and Malhan et al. 2022 used a coordinate system where prograde orbits are those with v_ϕ, $L_z < 0$.

[2]The mean of [Mg/Fe] and [Ca/Fe] values is taken as the [α/Fe] of programme stars, that are 0.57 and 0.58 in HE 0038 − 0345 and HE 1243 − 2408, respectively.

Aguado D. S. et al., 2021, ApJ, 908, L8
Amorisco N. C., 2017, MNRAS, 464, 2882
Andrievsky S. M., Spite M., Korotin S. A., Spite F., Bonifacio P., Cayrel R., Hill V., François P., 2007, A&A, 464, 1081
Aoki W., Ryan S. G., Norris J. E., Beers T. C., Ando H., Tsangarides S., 2002, ApJ, 580, L1149
Aoki W. et al., 2005, ApJ, 632, L611
Aoki W., Beers T. C., Christlieb N., Norris J. E., Ryan S. G., Tsangarides S., 2007, ApJ, 655, L492
Aoki W., Matsuno T., Honda S., Ishigaki M. N., Li H., Suda T., Kumar Y. B., 2018, PASJ, 70, 94
Arentsen A., Starkenburg E., Shetrone M. D., Venn K. A., Depagne É., McConnachie A. W., 2019, A&A, 621, 108
Asplund M., Grevesse N., Sauval A. J., Scott P., 2009, ARA&A, 47, 481
Babusiaux C. et al., 2023, A&A, 674, A32
Banerjee P., Qian Y.-Z., Heger A., 2018, ApJ, 865, L120
Beers T. C., 1999, in Gibson B. K., Axelrod R. S., Putman M. E.eds, Astronomical Society of the Pacific Conference Series Vol. 165, The Third Stromlo Symposium: The Galactic Halo. p. 202
Beers T. C., Christlieb N., 2005, ARA&A, 43, 531
Beers T. C. et al., 2007, ApJS, 168, 128
Beers T. C. et al., 2017, ApJ, 835, L81
Belokurov V., Erkal D., Evans N. W., Koposov S. E., Deason A. J., 2018, MNRAS, 478, 611
Bennett M., Bovy J., 2019, MNRAS, 482, 1417
Bensby T., Feltzing S., Lundström I., 2003, A&A, 410, 527
Bensby T., Feltzing S., Lundström I., 2004, A&A, 415, 155
Bessell M. S., Castelli F., Plez B., 1998, A&A, 333, 231
Bonifacio P. et al., 2015, A&A, 579, 28
Bovy J., 2015, ApJS, 216, 29
Bovy J. et al., 2012, ApJ, 759, L131
Buder S. et al., 2018, MNRAS, 478, 4513
Carollo D. et al., 2007, Nature, 450, 1020
Carollo D. et al., 2012, ApJ, 744, L195
Castelli F., Kurucz R. L., 2003, in Piskunov N., Weiss W. W., Gray D. F.eds, Proceedings of the IAU Symp. No 210 Vol. 210, Modelling of Stellar Atmospheres. p. A20
Chiaki G., Tominaga N., Nozawa T., 2017, MNRAS, 472, 115
Chiaki G., Susa H., Hirano S., 2018, MNRAS, 475, 4378
Choplin A., Hirschi R., Meynet G., Ekström S., 2017, A&A, 607, 3
Clarkson O., Herwig F., Pignatari M., 2018, MNRAS, 474, 37
Collet R., Asplund M., Trampedach R., 2007, A&A, 469, 687
Cooke R. J., Madau P., 2014, ApJ, 791, L116
Deason A. J., Belokurov V., Evans N. W., Johnston K. V., 2013, ApJ, 763, L113
Dietz S. E., Yoon J., Beers T. C., Placco V. M., 2020, ApJ, 894, L34
Dietz S. E., Yoon J., Beers T. C., Placco V. M., Lee Y. S., 2021, ApJ, 914, L100
Dobrovolskas V., Kučinskas A., Steffen M., Ludwig H. G., Prakapavičius D., Klevas J., Caffau E., Bonifacio P., 2013, A&A, 559, 102
Ezzeddine R. et al., 2019, ApJ, 876, L97
Forbes D. A., 2020, MNRAS, 493, 847
Frebel A., Ji A. P., 2023, preprint (arXiv:2302.09188)
Frebel A., Norris J. E., 2015, ARA&A, 53, 631
Frebel A. et al., 2006, ApJ, 652, L1585
Frebel A., Collet R., Eriksson K., Christlieb N., Aoki W., 2008, ApJ, 684, L588
Frischknecht U., Hirschi R., Thielemann F. K., 2012, A&A, 538, 2
Gaia Collaboration, 2016, A&A, 595, 1
Gaia Collaboration: Vallenari A. et al., 2023, A&A, 674, A1
Girardi L., Bressan A., Bertelli G., Chiosi C., 2000, A&AS, 141, 371
Goswami P. P., Rathour R. S., Goswami A., 2021, A&A, 649, 49
Gratton R. G., Sneden C., Carretta E., Bragaglia A., 2000, A&A, 354, 169
Hansen T. et al., 2015, ApJ, 807, L173
Hansen T. T., Andersen J., Nordström B., Beers T. C., Placco V. M., Yoon J., Buchhave L. A., 2016a, A&A, 586, 160
Hansen T. T., Andersen J., Nordström B., Beers T. C., Placco V. M., Yoon J., Buchhave L. A., 2016b, A&A, 588, 3

Hansen C. J. et al., 2016c, A&A, 588, 37
Hansen C. J., Hansen T. T., Koch A., Beers T. C., Nordström B., Placco V. M., Andersen J., 2019, A&A, 623, 128
Hartwig T., Bromm V., Klessen R. S., Glover S. C. O., 2015, MNRAS, 447, 3892
Hartwig T. et al., 2018, MNRAS, 478, 1795
Hayek W., Asplund M., Collet R., Nordlund Å., 2011, A&A, 529, 158
Heger A., Woosley S. E., 2010, ApJ, 724, L341
Helmi A., 2020, ARA&A, 58, 205
Helmi A., Babusiaux C., Koppelman H. H., Massari D., Veljanoski J., Brown A. G. A., 2018, Nature, 563, 85
Holmbeck E. M. et al., 2020, ApJS, 249, 30
Honda S., Aoki W., Kajino T., Ando H., Beers T. C., Izumiura H., Sadakane K., Takada-Hidai M., 2004, ApJ, 607, L474
Horta D. et al., 2021, MNRAS, 500, 1385
Jablonka P. et al., 2015, A&A, 583, 67
Jeon M., Besla G., Bromm V., 2017, ApJ, 848, L85
Jeon M., Bromm V., Besla G., Yoon J., Choi Y., 2021, MNRAS, 502, 1
Johnson D. R. H., Soderblom D. R., 1987, AJ, 93, 864
Johnson J. A., Herwig F., Beers T. C., Christlieb N., 2007, ApJ, 658, L1203
Kim Y. K., Lee Y. S., Beers T. C., 2019, ApJ, 882, L176
Koch-Hansen A. J., Hansen C. J., Lombardo L., Bonifacio P., Hanke M., Caffau E., 2021, A&A, 645, 64
Komiya Y., Suda T., Minaguchi H., Shigeyama T., Aoki W., Fujimoto M. Y., 2007, ApJ, 658, L367
Koppelman H., Helmi A., Veljanoski J., 2018, ApJ, 860, L11
Koppelman H. H., Helmi A., Massari D., Price-Whelan A. M., Starkenburg T. K., 2019, A&A, 631, 9
Korn A. J., Grundahl F., Richard O., Mashonkina L., Barklem P. S., Collet R., Gustafsson B., Piskunov N., 2007, ApJ, 671, L402
Kruijssen J. M. D., Pfeffer J. L., Reina-Campos M., Crain R. A., Bastian N., 2019, MNRAS, 486, 3180
Kruijssen J. M. D., et al., 2020, MNRAS, 498, 2472
Lee Y. S. et al., 2013, AJ, 146, 132
Lombardo L. et al., 2022, A&A, 665, 10
Maeder A., Meynet G., 2015, A&A, 580, 32
Malhan K. et al., 2022, ApJ, 926, L107
Mardini M. K. et al., 2022, MNRAS, 517, 3993
Mashonkina L., Jablonka P., Pakhomov Y., Sitnova T., North P., 2017, A&A, 604, 129
Matsuno T., Aoki W., Suda T., 2019, ApJ, 874, L35
Meynet G., Ekström S., Maeder A., 2006, A&A, 447, 623
Mishenina T. V., Soubiran C., Kovtyukh V. V., Korotin S. A., 2004, A&A, 418, 551
Miyamoto M., Nagai R., 1975, PASJ, 27, 533
Mucciarelli A., Bonifacio P., 2020, A&A, 640, 87
Myeong G. C., Evans N. W., Belokurov V., Sanders J. L., Koposov S. E., 2018, ApJ, 856, L26
Myeong G. C., Vasiliev E., Iorio G., Evans N. W., Belokurov V., 2019, MNRAS, 488, 1235
Naidu R. P., Conroy C., Bonaca A., Johnson B. D., Ting Y.-S., Caldwell N., Zaritsky D., Cargile P. A., 2020, ApJ, 901, L48
Naidu R. P. et al., 2022, ApJ, 926, L36
Navarro J. F., Frenk C. S., White S. D. M., 1996, ApJ, 462, L563
Nomoto K., Kobayashi C., Tominaga N., 2013, ARA&A, 51, 457
Norris J. E., Yong D., 2019, ApJ, 879, L37
Norris J. E. et al., 2013, ApJ, 762, L25
Pfeffer J., Lardo C., Bastian N., Saracino S., Kamann S., 2021, MNRAS, 500, 2514
Pillepich A. et al., 2014, MNRAS, 444, 237
Placco V. M., Frebel A., Beers T. C., Stancliffe R. J., 2014, ApJ, 797, L21
Placco V. M. et al., 2016, ApJ, 833, L21
Placco V. M., Sneden C., Roederer I. U., Lawler J. E., Den Hartog E. A., Hejazi N., Maas Z., Bernath P., 2021, Research Notes of the American Astronomical Society, 5, 92
Pols O. R., Izzard R. G., Stancliffe R. J., Glebbeek E., 2012, A&A, 547, 76
Purandardas M., Goswami A., 2021a, ApJ, 912, L74
Purandardas M., Goswami A., 2021b, ApJ, 922, L28

Purandardas M., Goswami A., Goswami P. P., Shejeelammal J., Masseron T., 2019, MNRAS, 486, 3266

Purandardas M., Goswami A., Shejeelammal J., Sonamben M., Pawar G., Mkrtichian D., Doddamani V. H., Joshi S., 2022, MNRAS, 513, 4696

Raskin G. et al., 2011, A&A, 526, 69

Reddy B. E., Lambert D. L., Allende Prieto C., 2006, MNRAS, 367, 1329

Roederer I. U., Preston G. W., Thompson I. B., Shectman S. A., Sneden C., Burley G. S., Kelson D. D., 2014, AJ, 147, 136

Roederer I. U., Sneden C., Lawler J. E., Sobeck J. S., Cowan J. J., Boesgaard A. M., 2018, ApJ, 860, L125

Salvadori S., Ferrara A., 2009, MNRAS, 395, 6

Salvadori S., Schneider R., Ferrara A., 2007, MNRAS, 381, 647

Salvadori S., Skúladóttir Á., Tolstoy E., 2015, MNRAS, 454, 1320

Schönrich R., Binney J., Dehnen W., 2010, MNRAS, 403, 1829

Shejeelammal J., Goswami A., 2021, ApJ, 921, L77

Shejeelammal J., Goswami A., 2022, ApJ, 934, L110

Shejeelammal J., Goswami A., Goswami P. P., Rathour R. S., Masseron T., 2020, MNRAS, 492, 3708

Shejeelammal J., Goswami A., Shi J., 2021, MNRAS, 502, 1008

Simpson J. D., Martell S. L., 2019, MNRAS, 490, 741

Sneden C. A., 1973, PhD thesis, The University of Texas at Austin.

Spite M. et al., 2005, A&A, 430, 655

Spite M. et al., 2006, A&A, 455, 291

Spite M., Caffau E., Bonifacio P., Spite F., Ludwig H. G., Plez B., Christlieb N., 2013, A&A, 552, 107

Spite M., Spite F., François P., Bonifacio P., Caffau E., Salvadori S., 2018, A&A, 617, 56

Starkenburg E., Shetrone M. D., McConnachie A. W., Venn K. A., 2014, MNRAS, 441, 1217

Starkenburg E., Oman K. A., Navarro J. F., Crain R. A., Fattahi A., Frenk C. S., Sawala T., Schaye J., 2017, MNRAS, 465, 2212

Tafelmeyer M. et al., 2010, A&A, 524, 58

Tominaga N., Iwamoto N., Nomoto K., 2014, ApJ, 785, L98

Umeda H., Nomoto K., 2003, Nature, 422, 871

Umeda H., Nomoto K., 2005, ApJ, 619, L427

Venn K. A., Irwin M., Shetrone M. D., Tout C. A., Hill V., Tolstoy E., 2004, AJ, 128, 1177

Vincenzo F., Matteucci F., Vattakunnel S., Lanfranchi G. A., 2014, MNRAS, 441, 2815

Wang W., Han J., Cautun M., Li Z., Ishigaki M. N., 2020, Science China Physics, Mechanics, and Astronomy, 63, 109801

Watkins L. L., van der Marel R. P., Sohn S. T., Evans N. W., 2019, ApJ, 873, L118

Woody T., Schlaufman K. C., 2021, AJ, 162, 42

Yong D. et al., 2013, ApJ, 762, L26

Yoon J. et al., 2016, ApJ, 833, L20

Yoon J. et al., 2018, ApJ, 861, L146

Yoon J., Beers T. C., Tian D., Whitten D. D., 2019, ApJ, 878, L97

Yoon J., Whitten D. D., Beers T. C., Lee Y. S., Masseron T., Placco V. M., 2020, ApJ, 894, L7

Zepeda J. et al., 2023, ApJ, 947, L23

de Bennassuti M., Salvadori S., Schneider R., Valiante R., Omukai K., 2017, MNRAS, 465, 926

APPENDIX A: LINE LIST

The lines used to derive the elemental abundances are listed in Tables A1 – A2.

Table A1. Equivalent widths (in mÅ) of Fe lines used for deriving atmospheric parameters.

Wavelength (Å)	El	E_{low}(eV)	log gf	HE 0038 − 0345	HE 1243 − 2408
4132.9	Fe I	2.84	−0.920	28.5(4.59)	−
4153.90		3.40	−0.280	−	18.4(4.26)
4337.05		1.56	−1.7	−	63.4(4.63)
4489.74		0.12	−3.90	40.9(4.54)	−
4547.847		3.546	−0.820	−	8.2(4.51)
5005.711		3.883	−0.120	17.5(4.59)	−
5006.119		2.833	−0.61	−	38.1(4.33)
5151.911		1.010	−3.320	−	22.2(4.45)
5198.711		2.222	−2.135	−	14.8(4.55)
5215.179		3.266	−0.933	−	14.2(4.48)
5226.862		3.038	−0.667	−	28.5(4.28)
5263.31		3.260	−0.870	−	13.4(4.42)
5339.93		3.27	−0.680	27.3(4.64)	−
5364.870		4.44	0.220	−	10.4(4.56)
5393.17		3.24	−0.720	24.8(4.64)	−
5569.62		3.42	−0.490	−	22.5(4.52)
5586.76		3.370	−0.110	36.8(4.45)	−
6137.694		2.588	−1.403	−	23.1(4.39)
6219.28		2.200	−2.450	−	8.8(4.46)
6252.555		2.402	−1.690	−	23.0(4.45)
6393.60		2.430	−1.620	30.7(4.65)	−
6430.85		2.18	−2.010	29.1(4.63)	22.4(4.40)
4233.16	Fe II	2.580	−2.020	−	32.8(4.42)
4416.820		2.780	−2.570	11.2(4.61)	−
4491.405		2.855	−2.700	6.6(4.56)	−
4508.288		2.855	−2.210	−	16.1(4.59)
4520.224		2.81	−2.600	8.4(4.56)	7.4(4.35)

Note. The numbers in the parenthesis in columns 5 and 6 give the derived absolute abundances from the respective line.

Table A2. Equivalent widths (in mÅ) of lines used for deriving elemental abundances.

Wavelength (Å)	Element	E_{low}(eV)	log gf	HE 0038 − 0345	HE 1243 − 2408
5682.633	Na I	2.102	−0.700	8.3(4.20)	–
4702.991	Mg I	4.346	−0.666	44.3(5.26)	53.8(5.48)
5528.405		4.346	−0.620	57.0(5.44)	50.8(5.30)
5948.541	Si I	5.083	−1.23	6.9(5.41)	–
4098.530	Ca I	2.530	−0.520	12.9(4.07)	–
4283.011		1.886	−0.224	–	28.8(3.54)
4455.890		1.899	−0.540	–	23.9(3.73)
5594.462		2.523	−0.050	23.3(3.70)	–
6102.723		1.879	−0.890	–	16.9(3.66)
6162.173		1.899	0.1	57.6(4.08)	–
6439.075		2.525	0.47	43.4(3.90)	31.1(3.57)
6493.781		2.521	0.14	17.8(3.70)	19.2(3.49)
4533.239	Ti I	0.848	0.476	–	32.3(2.20)
4999.50		0.820	0.170	29.3(2.40)	–
5007.21		0.82	0.17	33.1(2.57)	33.3(2.50)
5210.386		0.047	−0.884	–	22.1(2.32)
4470.86	Ti II	1.16	−2.28	–	20.1(2.35)
4493.51		1.08	−2.73	15.3(2.70)	–
5185.9		1.89	−1.35	21.7(2.43)	–
5226.543		1.566	−1.300	47.9(2.64)	33.8(2.12)
5336.77		1.58	−1.700	–	29.9(2.43)
5381.015		1.566	−2.08	20.7(2.56)	26.7(2.73)
4289.73	Cr I	0.00	−0.37	78.2(2.97)	67.1(2.48)
5206.04		0.94	0.020	–	51.4(2.46)
5345.801		1.003	−0.980	–	12.8(2.39)
5409.772		1.03	−0.720	30.3(2.69)	26.5(2.56)
4855.41	Ni I	3.54	0.000	9.7(3.46)	–
4904.41		3.54	−0.170	–	3.1(3.08)
5084.08		3.68	0.030	–	–
5115.39		3.83	−0.110	–	2.0(3.15)
5146.48		3.706	0.12	7.5(3.38)	–
4722.15	Zn I	4.029	−0.370	–	8.1(1.88)
4810.53		4.08	−0.170	17.9(2.20)	–

Note. The numbers in the parenthesis in columns 5 and 6 give the derived absolute abundances from the respective line.

This paper has been typeset from a TEX/LATEX file prepared by the author.